SEVENTH FRAMEWORK PROGRAMME

Report on Y3 activities

FP7-ICT-216863/ORC/R/PU/D15.3

Project Number: FP7-ICT-2007-1 216863

Project Title: Building the Future Optical Network in Europe (BONE)

Contractual Date of Deliverable: 31/12/10

Actual Date of Delivery: 18/01/11

Workpackage contributing to the Deliverable: WP15 : VCE Transmission Techniques

Nature of the Deliverable Make your choice from: R

Dissemination level of Deliverable Make your choice from: PU

Editors: Partner / names

Francesca Parmigiani ORC
Periklis Petropoulos ORC

Abstract:

This deliverable reports the activities of the Virtual Centre of Excellence on Transmission Techniques, and the progress achieved during Year 3 of the project.

Keyword list: Optical communications, 100Gb/s transmission, coherent systems, regeneration, highly nonlinear fibres, semiconductor optical amplifiers, erbium doped fibre amplifiers, burst amplification, signal monitoring, Gigabit Ethernet, fibre Bragg gratings, reliability analysis

Clarification:

Nature of the Deliverable

R	Report
P	Prototype
D	Demonstrator
O	Other

Dissemination level of Deliverable:

PU	Public
PP	Restricted to other programme participants (including the Commission Services)
RE	Restricted to a group specified by the consortium (including the Commission Services)
CO	Confidential, only for members of the consortium (including the Commission Services)

Disclaimer

The information, documentation and figures available in this deliverable, is written by the BONE ("Building the Future Optical Network in Europe*) – project consortium under EC co-financing contract FP7-ICT-216863 and does not necessarily reflect the views of the European Commission*

Table of Contents

1. Executive Summary

This document provides a presentation of the activities of the Virtual Centre of Excellence in Transmission Techniques (VCE-T) during the third and final year of the BONE project. After a brief introduction and an outline of the management activities of the WP, the technical contributions to this report are presented in detail, highlighting the collaborative and joint activities that have been carried out.

2. Introduction

FPMs	HHI	UCL	UPVLC	FT	ICCS-NTUA	GET
UoA	HWDU	POLITO	UPC	FUB	TID	Ericsson
ISCOM	AIT	TUE	IT	PUT	KPRC/ ACREO	ORC
UEssex	USWAN	CTTC	UNIROMA3	UC3M	UOP	CORITEL

Table 1: Acronyms of the VCE-T partners

The aim of the Virtual Centre of Excellence on Transmission Techniques (VCE-T) is to organize and harmonize the transmission-related activities within the BONE project. Table 1 shows the project partners who have been more active in the discussions and technical activities of the workpackage during the three years of the project, as reflected by their participation in the WP meetings and the work reported in this deliverable. The coordination of the WP activities is taken care by the leadership team (Periklis Petropoulos and Francesca Parmigiani, ORC) with the help and consultation of the Advisory Board (AB) of VCE-T. Since the theme of Transmission in Optical Systems is rather broad, the interests of the various partners vary significantly. In order to address the varying background and interests of the partners participating in VCE-T, an extensive AB has been put in place since the start of the VCE-T activities. The AB has been responsible for setting out and updating the integration strategy for the WP and monitoring the progress made towards achieving its goals. The members of the AB and their affiliations are shown below:

Periklis Petropoulos (WP leader) and Francesca Parmigiani (ORC)

Patrice Megret (FPMs)

Karin Ennser (SWANSEA)

Pierluigi Poggiolini (POLITO)

Giorgio Maria Tosi Beleffi (ISCOM)

Michel Morvan (GET)

Oscar Gonzalez (TID)

Erwan Pincemin (FT)

From an early stage in the formation of VCE-T, its main activities have been grouped into broad research themes, forming Focus Groups. The Focus Groups have acted as common forums of discussion within the WP, eventually leading to joint activities between their participants. Although these themes reflect broad areas of research on transmission, which are shared among several of the VCE participants, they are not exclusive, as will become evident further into this deliverable. Additional joint activities are encouraged and monitored within VCE-T, and are used to dynamically steer the emphasis of the Focus Groups. A discussion on the definition of the topics included within the various Focus Groups is revisited regularly, mainly during the WP general meetings.

VCE-T participants have met twice during Year 3 of the project, in coincidence of the two following conferences: 12th International Conference on Transparent Optical Networks, held in Munich, Germany, on June27-July 12, and 36th European Conference and Exhibition on Optical Communication (ECOC), held in Turin, Italy, on September 19 - 23, 2010. In this final year of the project, the main discussions in the WP meetings have mainly focused on the final planning of the VCE-T book, which is to be published shortly.

2.1 Outline of the report

The aim of this deliverable is to report the actions taken during this past year towards fostering integration of the BONE groups working on transmission-related issues. It also provides a comprehensive presentation of the technical activities carried out during Y3, highlighting the high level of collaboration achieved among the various partners in the workpackage. The report is organised as follows.

Section 3 presents the central activities carried out within the WP in order to facilitate integration among the VCE-T participants and organise the joint activities in the WP. It also reviews briefly the topics of the Focus Groups, as these had been defined from the start of the project and reviewed during its course. Some quantifiable measures of integration are outlined in this Section.

Sections 4-6 relate to the technical activities of each of the Focus Groups. Section 4 relates to issues associated with high speed transmission, Section 5 is on signal regeneration and Section 6 is on signal monitoring. Two more activities which fall within the VCE-T interests, and which follow from work carried out in the earlier years of the project are presented in Section 7. It is noted that some single-partner activities which have been the subject of discussion and have informed other work within VCE-T are also reported. The report closes with some Conclusions in Section 8.

3. Management Activities

As in the previous project years, the central activities taking place within VCE-T have been organized so as to create a forum of discussion for certain key research topics within Optical Transmission which are common to several WP partners, and encourage collaboration between the various groups participating in the WP. These activities act as a vehicle to facilitate joint actions between the participating groups, and are presented below. Mention is also given in this Section to the results achieved in terms of integration during this third year, as these can be quantified in terms of mobility actions, joint publications, etc.

3.1 WP Technical Meetings

The VCE-T partners have decided in the previous years to produce a book which would stem from the work conducted within BONE. Preparations of this book have intensified during the last year of the project and consequently, most discussions during the two project meetings of the year have focused on its progress.

The two VCE-T meetings of the year were collocated with ICTON'2010 (Munich, Germany, June 2010) and ECOC'2010 (Turin, Italy, September 2010) respectively. The meeting at ICTON'2010 concentrated more on executive decisions of the editorial board of the book and followed a period of frequent email collaboration between its members. The meeting at ECOC included more VCE-T partners and was helpful in adjusting some of the contents of the book and deciding on guidelines for action.

3.2 Focus Groups

As reported in deliverables D15.1 and D15.2, four Focus Groups have been formed in VCE-T, in order to facilitate a thematic context of the core activities in the WP. These groups have been (a) Key Issues in 100Gbit/s transmission; (b) Signal regeneration; (c) Amplification in Transmission; and (d) Monitoring. Due to lack of continued interest in the topic, the Focus Group on Amplification has not been active in Y3 (a small number of publications that emerged this year reported on work that had been carried out previously). In addition, in order to reflect recent developments in transmission and the emphasis on complex modulation formats, we have broadened the scope of Focus Group (a) and renamed it to High-Speed Transmission. Section 4 presents the breadth of activities carried out within the scope of this Focus Group, with studies ranging from the accommodation of different modulation formats within the same transmission line to the development of maximum-likelihood sequence-estimation processing systems for differential quadrature phase-shift keying modulation. Focus Groups (b) Signal regeneration and (d) Monitoring have remained unaffected, reflecting the sustained interest of a number of VCE-T partners in these areas.

As ever, definition of the Focus Groups has not excluded activities in other transmission-related research areas. This is reflected in this report by the activities reported in Section 7, where some studies falling on the boundaries of some of the Focus Groups have been presented.

3.3 Quantifiable measures of integration

The number of joint activities accomplished with Y3 of VCE-T has increased significantly as compared to the previous years, as has the number of joint publications. In total, there have been ten mobility actions between partners, and a larger number of joint experiments (facilitated e.g. by the provision of special devices from one partner to another, the exchange of equipment, etc). According to the records that have been uploaded on the BONE Directory Service, there have been 37 papers in Y3, stemming from the various joint activities have already been accepted for publication in journals or conference proceedings. Joint papers from VCE-T partners have been published in such journals as Nature Photonics, Optics Letters, Photonics Technology Letters, as well as in conferences such as ECOC and OFC (including postdeadline papers).

Various joint activities in the VCE have attracted industrial interest. Typical examples include the involvement of Huawei and Ericsson (project partners) in the VCE-T activities, while several academic partners have actively engaged with companies, such as Oclaro, Cisco, Fastweb, OFS and Eblana Photonics, as will be evident in the technical sections of this report which follow.

3.3.1 VCE-T book

A large number of project partners have been interested in getting involved and contributing in the production of a book that would document some of the technical advances that have been achieved within VCE-T. Two project partners with a history of close collaboration (Giorgio Maria Tosi Beleffi, ISCOM and Antonio Teixeira, IT) have volunteered to the act as the editors for this document. They have been assisted by an active Editorial Board consisting of the following members: Periklis Petropoulos (ORC), Francesca Parmigiani (ORC), Ioannis Tomkos (AIT), Davide Forin (ISCOM), Franco Curti (ISCOM), Rogeiro Nogueira (IT), Marco Forzati (ACREO) and Josep Prat (UPC). The publishing house Springer has agreed to publish the book. Publication is scheduled for a few months after the end of the project.

The table of contents of the book is given below:

1 State of the art on transmission techniques

- 1.1 Introduction
- 1.2 Fibre channel characteristics
  - 1.2.1 Linear effects in optical fibres
  - 1.2.2 Nonlinear effects in optical fibres
- 1.3 Intensity and differential-phase modulation formats
  - 1.3.1 Intensity modulation
  - 1.3.2 Differential phase modulation
  - 1.3.3 Summary
- 1.4 Field modulation and coherent detection
  - 1.4.1 Coherent receiver architecture
    - 1.4.1.1 Carrier phase estimation
    - 1.4.1.2 Dispersion compensation
    - 1.4.1.3 Polarisation tracking and PMD compensation

3.4.1 IM-DD systems

3.4.2 RZ-DPSK

3.4.3 RZ DQPSK systems

3.5 Simulation results for long haul transmission systems

3.5.1 The limits of the Chromatic Dispersion for Optical Communication system

3.5.2 Chromatic dispersion compensation by means of Kerr nonlinearity: the soliton case

Fiber loss

ASE noise

Polarization mode dispersion

Chromatic dispersion fluctuation and dispersion management

WDM systems

3.5.3 Simulations for links with dispersion management

3.5.3.1 Theory on dispersion management for phase modulated signals

3.5.3.2 Results on precompensation effect on DPSK and DQPSK

3.5.3.3 Comparison at 100 Gb/s

3.6 Propagation in the presence of in-line All Optical Devices

4. Experiments on long high capacity transmission systems

4.1 Introduction

4.2 100 Gb/s PM-QPSK WDM Transmission Experiments over Installed Fiber

4.3 Transoceanic PM-QPSK Terabit Superchannel Transmission Experiments

4.4 Experimental investigation on 100 Gb/s POLMUX including All Optical Wavelength Conversion

4.5 The current status of long haul high bit rate transmission experiments: results from ECOC 2010

4.6 Experimental Investigation of WDM Burst Traffic Amplification

5. Economics of Next Generation Networks

5.1. The cost side: Techno-economics of Future Internet

5.1.1. Backbone networks and cost analysis theory

5.1.2. Case studies for metro and access networks

5.2. The benefit side: The economic impact of Future Internet

5.2.1. Socio-economic gains

5.3. Future Internet and new business models

5.3.1. The Open Network Model

5.3.2. Blue Ocean Strategies

Several challenges had to be overcome during this effort, mainly associated with the limited lifetime and the low level of resources available within BONE; the amount of effort required from the editorial and the authoring teams in order to complete the task; and the necessity to harmonise the heterogeneous content of the various partners’ contributions. Overall, the task would not be completed without the professional effort of a large number of contributors. At the same time, inevitably a small number of partners who have failed to deliver what had been promised, greatly compromised the total effort.

The following sections of this report outline the results of some joint activities which have taken place during Y3 of the project. They are thematically divided into the various Focus Groups which have been defined within VCE-T. Therefore, Section 4 reports on activities relating to high-speed transmission, Section 5 on regeneration and Section 6 on monitoring. Finally, Section 7 reports some other transmission-related activities which do not explicitly fall within the remit of any of the Focus Groups.

4. High Bit-Rate Transmission (PoliTO, HWDU, UCL, ICCS/NTUA, AIT, FUB)

4.1 MLSE-Based DQPSK Transmission in 43 Gb/s DWDM Long-Haul Dispersion-Managed Optical Systems (PoliTO-HWDU)

In the context of the study of the use of maximum-likelihood sequence-estimation (MLSE) processors in optical transmission systems, we analyzed by simulation the performance of Differential Quadrature Phase Shift Keying (DQPSK) modulation using a 64-state joint-symbol MLSE receiver (Rx) [1, 2] in a long-haul dispersion-managed multi-span dense wavelength division multiplexed (DWDM) optical system with 50 GHz channel spacing, operating in the non-linearity-limited regime. We chose to test the system by increasing the span loss and the launch power, while keeping the number of spans fixed (20 in all). We varied both the in-line and total dispersion residues across a large range of values, using either a conventional DQPSK Rx or an MLSE Rx. We tested both a conventional MLSE processor and a noise correlation-sensitive (CS) processor. Then, we accurately assessed the extent of the advantage of using an MLSE Rx vs. a conventional Rx. The choice of 64 states for the MLSE processor was based on the fact that the current state-of-art is 16 states [3] and it is conceivable that a next-generation processor can reach 64.

4.1.1 Simulation Set-Up

The DWDM system is composed of 9 optical channels, centered at a frequency f_0=194 THz, corresponding to the laser emission frequency of the center channel. The channel frequency spacing is Δf=50 GHz. The outputs of the 9 transmitters are combined and input to an EDFA pre-amplifier which is used to tune the launch power to $P_{TX} = 9 \cdot P_{ch}$, where P_{ch} is the average power per channel.

The transmission link is composed of 20 spans of standard single-mode fiber (SSMF), each of length L_{span}, with loss coefficient α = 0.22 dB/km, dispersion parameter D = 16.7 ps/(nm·km), and nonlinear coefficient $\gamma = 1.32\ W^{-1}km^{-1}$, corresponding to a nonlinear refractive index equal to $2.6 \cdot 10^{-20}$ and a core effective area of 80 μm^2.

Each fiber span is followed by an in-line dispersion compensating unit (DCU), which compensates for an amount of CD equal to D_{IL}, and by an in-line EDFA amplifier, which completely recovers the span loss, with noise figure equal to 5.5 dB. We assumed that the DCU would be inserted amidst a dual-stage EDFA, thus generating neither OSNR degradation nor further non-linearity. Pre- and post-compensation units are present as well, with dispersion parameters equal to D_{pre} and D_{post} respectively.

Dispersion maps are characterized using the inline and total dispersion compensation residues, respectively defined as:

$$R_{IL} = D_{IL} + D \cdot L_{span}$$

$$R_{tot} = D_{post} + D_{pre} + N_{span} \cdot R_{IL}$$

where N_{span} is the number of spans, equal to 20 in our simulations.

A typical DQPSK transmitter structure [4] is used. A Pseudo-Random Quaternary-Sequence (PRQS) generator [5] is used to produce a sequence of $2^{16} - 1$ symbols at a baud-rate of 21.5 Gbaud, corresponding to a bit-rate equal to 43 Gb/s. Each symbol is composed of 2 bits, corresponding to the in-phase and quadrature components of the DQPSK signal constellation [6]. Because of the differential nature of decoding in DQPSK, a precoding function is required at the transmitter to provide a direct mapping of data from the input to the output [4]. Different and uncorrelated PRQSs have been used for the 9 WDM channels.

The two parallel MZ modulators are biased for minimum optical transmission and driven with an NRZ binary signal filtered by a low-pass electrical filter. The driving voltage is in the range $[-V_\pi, V_\pi]$. The signals from the upper and lower branch are then recombined through an optical coupler, after adding an optical phase shift equal to $\pi/2$ to the upper branch. The shaping electrical filters are 5-pole Bessel with bandwidth $0.75 \cdot R_s$ (16 GHz), where R_s is the baud rate. Optical filtering is assumed to be present both at the transmitter (Tx) and at the Rx side, using second-order super-Gaussian optical filters with a -3 dB bandwidth of 35 GHz. The Rx optical filter is centered around f_0 = 194 THz in order to select the center channel that is used for BER measurement.

At the Rx side, the optical filter, tuned at the frequency of the center channel in order to analyze the worst case, is followed by a pair of asymmetric Mach-Zehnder (AMZ) interferometers with a differential delay equal to the time duration of a transmitted symbol, each followed by a balanced photo-detector (BPD) consisting of two photodiodes (one for each output branch of the AMZs), connected so as to subtract their currents from each other, then followed by a post-detection (PD) electrical filter. The differential optical phase between the interferometer arms is set to $\pi/4$ and - $\pi/4$ for the upper and lower branches respectively. The post-detection filters are 5-pole Bessel with bandwidth $0.75 \cdot R_s$ (16 GHz).

The two outputs of the PD filters, carrying the information about the in-phase and quadrature components of the DQPSK signal, respectively, are either fed to a pair of independent threshold Rx's or to a joint-symbol MLSE processor.

4.1.2 Simulation results

Following a similar approach to [7], we estimated over a large variety of dispersion maps the maximum tolerable span loss $A_{span}|$dB, i.e., the span loss which still allowed to achieve the reference bit error rate BER= 10^{-3}. With such data we drew contour plots of $A_{span}|$dB vs. R_{IL} and R_{tot}. Clearly, the higher the value of $A_{span}|$dB, the better the performance granted by that map. In fact, it is easy to verify that, given a fixed OSNR, an increase in launch power would allow an identical increase in span loss. In linearity, this would also ensure no change in final BER, which would remain fixed at a, say, reference value BER_{ref}. However, if non-linearity were present, an increase in $P_{ch}|$dBm might not allow the same increase in Aspan|dB.

For each dispersion map, a total of 2^{17} symbols were simulated, using the first 2^{16} for trellis training and the remaining 2^{16} for direct Monte-Carlo BER counting. This corresponds to about 65 expected symbol errors at the target BER, ensuring an estimated BER 95% confidence interval of [0.8·BER, 1.25·BER]. In the plots shown in the following, this is translated into a maximum error of ±0.5 dB in the value of A_{span}.

We show in Figure 1 (left) the contour plot of A_{span} vs. in-line residue R_{IL} and total dispersion compensation residue R_{tot} for a value of launch power per channel P_{ch} equal to 2dBm, using an optimized threshold Rx. Note that only the contour lines for Aspan higher or equal to 10 dB are shown in the plot. The maximum A_{span} in this configuration is 25.5 dBm. The range of suitable dispersion maps is very narrow, i.e. the tolerance to dispersion map design is low. We show in Figure 1 (right) the contour plots of A_{span} vs. in-line R_{IL} and total dispersion compensation residue R_{tot} obtained in the same configuration, but now using a joint symbol MLSE Rx. It is evident, that MLSE helps to increase the tolerance to dispersion map design. The use of MLSE also opens up a new region of operation in the over-compensated regime ($R_{IL} < 0$), corresponding to negative values of optimum residual dispersion R_{tot}.

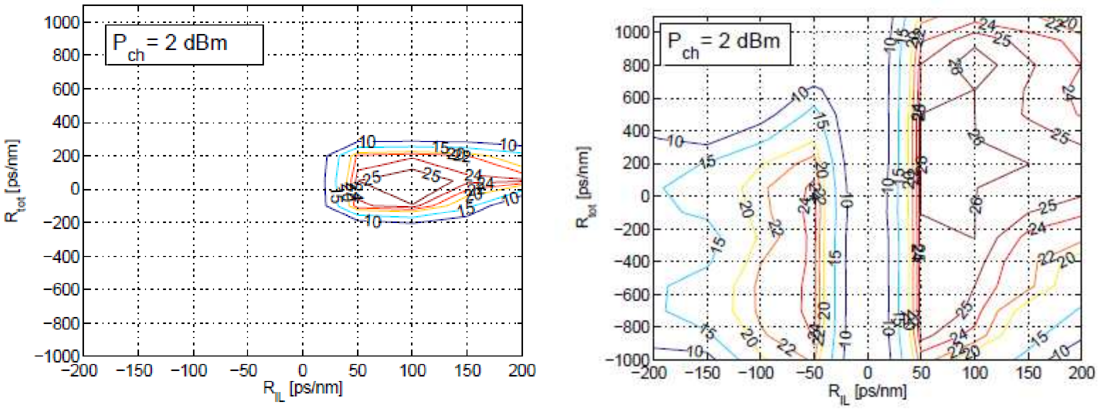

Figure 1. Performance of WDM 43 Gb/s DQPSK. Contour plots of maximum span loss Aspan (in dB) vs. in-line RIL and total dispersion compensation residue Rtot, with Dpre=-800 ps/nm, using a standard threshold receiver (left) and the 64-state joint- symbol MLSE Rx (right).

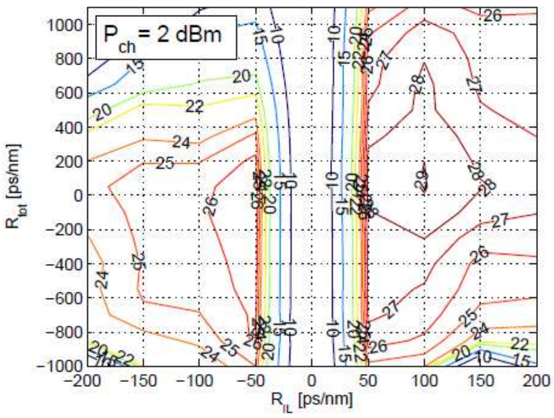

Figure 2. Performance of WDM 43 Gb/s DQPSK. Contour plots of maximum span loss Aspan (in dB) vs. in-line RIL and total dispersion compensation residue Rtot, with Dpre=-800 ps/nm, using a correlation-sensitive joint- symbol MLSE Rx with 64-states.

A way of further improving the performance and increasing the tolerance to the dispersion map of DQPSK is to use a noise correlation-sensitive (CS) MLSE Rx, i.e., a receiver which exploits the correlation between noise samples of adjacent symbols.

Figure 2 shows the results obtained using a 64-state CS-MLSE Rx, when P_{ch} = 2 dBm and D_{pre} = -800ps/nm. A comparison of this plot with the results obtained using the standard joint-symbol MLSE Rx shows that the use of the CS MLSE algorithm increases the maximum span loss from 26.5 dBm to 29 dBm. The tolerance to the dispersion map is further increased as well, especially in the region of negative in-line residues. This large difference hints at the fact that very substantial noise correlation is present in the signal. Since we are well into a non-linear regime, part of this correlation could be tentatively ascribed to non-linear disturbances too. For instance, it is known that XPM, depending on dispersion maps, may be subject to a form of ‘low-pass’ filtering which would then induce correlation [8]. If so, a CS MLSE processor is well-suited to take advantage of that.

4.1.3 Application to state-of-the-art systems

Currently, 43 Gb/s DQPSK is being deployed as a 10.7 Gb/s system replacement, worldwide. This is typically done over existing links whose dispersion maps were optimized for the pre-existing system. As an example, upgrades to 43 Gb/s are performed by using an additional tunable dispersion compensator in front of the receiver, than can be avoided by using an MLSE Rx which remarkably increases the range of total residual dispersion that can be tolerated by the system (from ±100 ps/nm to ±1000 ps/nm).

In a coherent Rx, the MLSE processor would certainly not be used to compensate for either CD or PMD, for which linear equalizers are better suited. Rather, it could be placed after the linear equalizers to try and mitigate intra-channel non-linearity and the correlated portion of inter-channel non-linearity. From the results of this paper, MLSE (and especially CS MLSE) appears to be able to improve system reach even in the non-linearity-limited test regime we used, operating at 2 dBm per channel. This hints at a potential use of MLSE techniques, especially with correlation-sensitivity, in the context of coherent systems too.

4.2 Long-haul Ultra-Dense WDM transmission using coherent receivers Over Uncompensated SMF and NZDSF (PoliTO-UCL)

A joint experimental activity involving PoliTO and UCL consisted of the investigation of long-haul reach of a 1.12-Tb/s DWDM system comprising 10 PM-QPSK modulated channels at 112 Gb/s (28 GBaud), spaced 1.1 times the Baud rate, using narrow optical filtering of the channels at the Tx. We tested both NZDSF and SMF. We also investigated by simulation the potential transmission reach when using LEAF and PSCF.

4.2.1 Experimental set-up

The experimental setup is shown in Figure 3. An external cavity laser source at 1549.6 nm with 100 kHz linewidth was modulated using a Nested Mach-Zehnder (NMZ) modulator to generate a 56 Gb/s QPSK signal, which was then narrow-filtered using a bandwidth-adjustable Finisar WaveShaper optical filter. The filter -3dB bandwidth delivering best performance was found to be 28 GHz, that is, equal to the Baud rate. The filter passband was also adjusted so as to have a 2-dB emphasis towards the filter sides, with respect to the center frequency. This was done to optically compensate for component bandwidth limitations in the system. The single modulated channel was then launched into a recirculating frequency-shifter (RFS) [9, 10]. The NMZ modulator inside the RFS loop was operated as a single-sideband modulator, configured to shift the input channel by a frequency which was set by a clock synthesizer to 30.8 GHz, chosen to obtain a channel spacing of 1.1 times the Baud rate. At each round in the RFS loop a new channel is generated, carrying uncorrelated data due to the loop delay. The RFS includes a 380 GHz optical filter whose high-frequency cut-off determines the number of channels generated, which in our experiment was 10. The optical signal was then polarization multiplexed to form a 1.12-Tb/s D-WDM aggregate. The measured D-WDM power spectrum is shown in Figure 4 (left). The single channel spectrum before filtering has the conventional NRZ shape.

The signal was then launched into a recirculating loop consisting of 100 km of uncompensated fiber. Two fiber types were tested: SMF with total loss 21 dB and dispersion D= 16.5 ps/nm/km; NZDSF with total loss 22 dB and D= 2.5 ps/nm/km. The loop included two EDFAs and an equalizing filter. At the required gain setting, the effective combined loop noise figure was 5.5 dB. For back-to-back sensitivity measurements, a noise-loading stage followed by a 5 nm optical filter was used at the coherent Rx input.

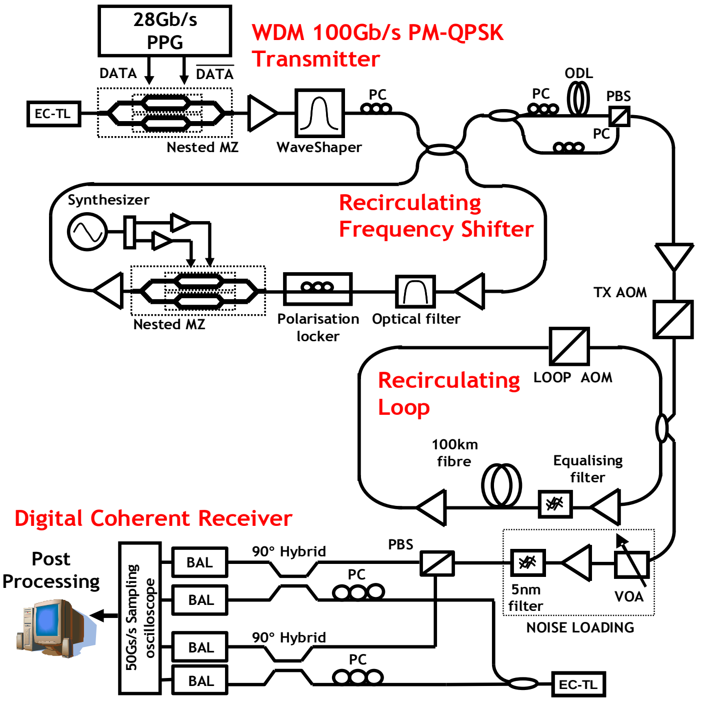

Figure 3. Experimental set-up for the generation, transmission and coherent detection of the 1.12 Tb/s 10-channels D-WDM system.

At the Rx, the signal was passed through a polarization beam splitter and then combined with the LO via two optical 90-degree hybrids to select the in-phase and quadrature components of the two polarizations. Note that channel selection at the Rx was performed by tuning the local oscillator (LO) laser and not by optical filtering. The eight outputs of the hybrids were detected using four amplified dual-balanced photo-receivers with 25 GHz bandwidth. On conversion into the electrical domain, the signal was digitized at 50 GSa/s (1.79 samples per symbol) using a real-time sampling scope with a measured -3dB bandwidth of 13 GHz. The sampled waveforms were then processed off-line in a conventional PC. The Rx digital signal processing was done as described in [11].

4.2.2 Experimental results

Figure 4 (right) shows the back-to-back (btb) BER performance measured on the 5th channel (the center one), as a function of the OSNR (over 0.1 nm). The OSNR for BER=$3\cdot10^{-3}$ was 16.5 dB. It was 3 dB higher than that of a single 112-Gb/s PM-QPSK channel measured without the WaveShaper optical filter and without the RFS, also shown in figure.

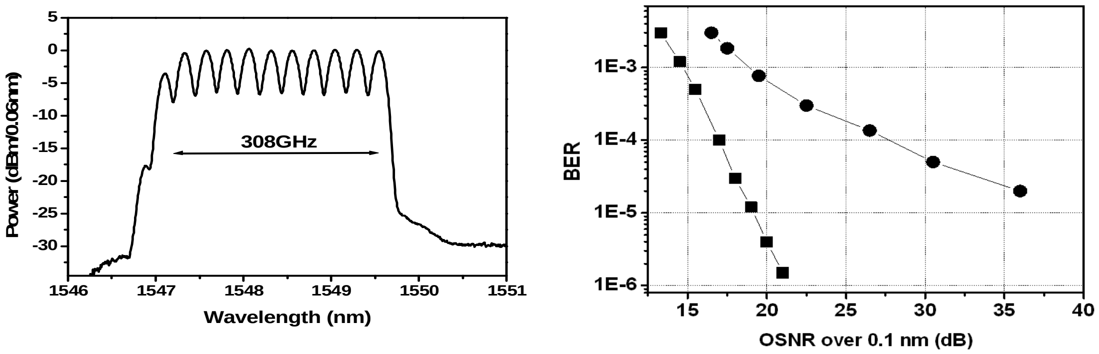

Figure 4. Left: transmitted D-WDM power spectrum with 10 channels at 30.8 GHz spacing, measured with a resolution of 0.06 nm (7.5 GHz). Right: Back-to-back BER vs. OSNR. Squares: single 112 Gb/s PM-QPSK channel without narrow optical filter and without RFS. Circles: D-WDM conditions, 5th channel, with narrow optical filter and RFS.

This 3-dB OSNR penalty was due to: the narrow filtering introduced by the WaveShaper (1 dB); the inter-channel crosstalk caused by the tight channel spacing (0.5 dB); the RFS (1.5 dB). Specifically, the RFS caused ASE noise accumulation in its loop and spurious inter-channel interference due to imperfectly suppressed higher optical harmonics generated in the RFS NMZ. This last effect was enhanced by the birefringence of the RFS components, which made optimal polarization alignment within the RFS difficult to ensure.

Figure 5 shows the maximum distance attainable for a BER of $3{\cdot}10^{-3}$ as a function of fiber launched power measured on the 5^{th} channel in the DWDM transmission environment over the recirculating loop. The maximum distance achieved with the NZDSF was 8 spans (800-km) which was greatly increased to 23 spans (2300-km) when using the SMF. The optimal power per channel for maximum reach was found to be about -0.5 dBm for the SMF and -3.5 dBm for the NZDSF. The substantially shorter reach observed with NZDSF is essentially attributable to non-linear effects which are enhanced by its smaller effective area. Also, the higher dispersion coefficient of the SMF appears to be quite beneficial for PM-QPSK systems [12].

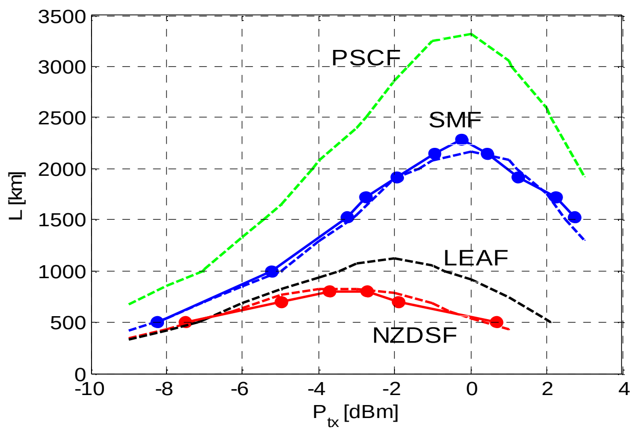

Figure 5. Transmission distance vs. fiber launch power per channel. Solid lines with markers: experimental results measured on the 5th channel, over SMF and NZDSF. Dashed lines: simulations over NZDSF, LEAF, SMF and PSCF.

Results obtained by simulation are also shown in Figure 5 (dashed curves). The fiber non-linear coefficient was set to γ=2 $W^{-1}km^{-1}$ for the NZDSF and γ=1.3 $W^{-1}km^{-1}$ for the SMF. The BER was estimated by error counting over a sequence of 2^{16} symbols. Different and uncorrelated PRBSs were used for all WDM channels. To match simulation and experimental results in linearity, a suitable amount of simulated ASE noise was inserted after the Tx. By doing this, a good agreement between simulation and experiment was found in the non-linear region too, for both fibers, as shown in Figure 5. Having tuned our Tx and Rx simulation set-up by matching it to the experiment, we added two more curves to predict performance with LEAF (total span loss 22 dB, D=3.8 ps/nm/km, γ=1.5 $W^{-1}km^{-1}$) and PSCF (total span loss 19 dB, D=20.6 ps/nm/km, γ=0.95 $W^{-1}km^{-1}$). Again, the span length was 100 km. The numerical predictions show that, using our experimental set-up, the 1.12 Tb/s DWDM system should be able to achieve 1100 km over LEAF and 3300 km over PSCF. The PSCF reach is about 40% farther than SMF, due to the PSCF lower non-linear coefficient, lower attenuation and slightly higher dispersion than SMF, all positive factors towards increasing reach.

In conclusion, we demonstrated a transmission distance of 2300 km over SMF. The system potential is however higher: experiment-matched simulations show that by removing the RFS impairments, which are not fundamental, a reach of 3300 km should be attainable over SMF. We also experimentally showed that conventional NZDSF is a suboptimum transmission medium for this type of DWDM system, reaching only 800 km. By simulations, we also found that LEAF should be about 40% better than NZDSF, and PSCF should be about 45% better than SMF, potentially reaching 3300 km with our set-up and up to 4900 km without RFS impairments. These results suggest that narrow-filtered DWDM channels might be a viable and effective solution for future long-haul core networks.

4.3 22-Gb/s OOK/DPSK Transmission Experiment (ICCS/NTUA, AIT)

In the frame of this joint activity, ICCS/NTUA in collaboration with AIT examined the transmission potential of multi-format modulated signals. At the transmitter side, an InP integrated IQ modulator, provided by HHI, was used to generate the Return-to-Zero OOK/DPSK modulated signals at the rate of 22 GHz. The appropriate modulation format was selected by the configuration of the modulator bias conditions. At the first stage of this experiment, the appropriate transmission test-bed was designed and implemented based on a configurable re-circulating loop setup as it is shown in Figure 1. The main study was focused on the optimization of the transmission link length, the dispersion compensation operating band as also the clock distribution concept.

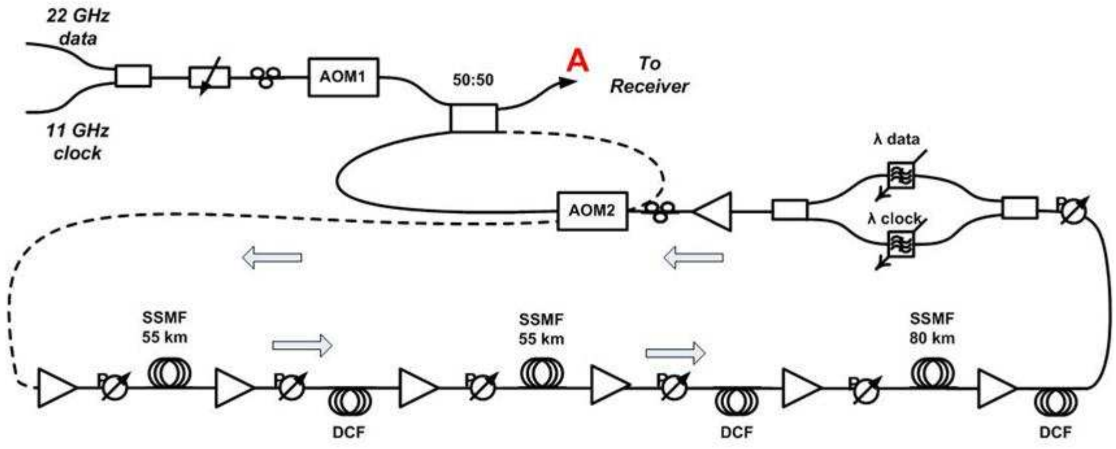

Figure 6. Re-circulating loop setup

As depicted in Figure 6, two Acousto-Optic Modulators (AOMs) were used at the input and the output of the optical link to control the flow of data inside the loop. Different span lengths of Single-Mode Fiber (SMF) and Dispersion-Compensated Fiber (DCF) were used with the appropriate input power for the best dispersion compensation and the maximum optical link length. In addition, at the output of the transmission link a filtering element was used in order to remove the accumulated and re-amplified noise spectrum from the EDFAs. An 11 GHz optical clock was transmitted through the same optical link additional to the modulated signal in order the relative drift of the two signals to be the same after the loop circulations, making with this way the extracted electrical clock necessary for the data signal detection. At the receiver side, the two signals were separated after the optical link. The modulated signal was forwarded for BER estimation whereas the clock signal was extracted for gate triggering the BER tester, as depicted in Figure 7.

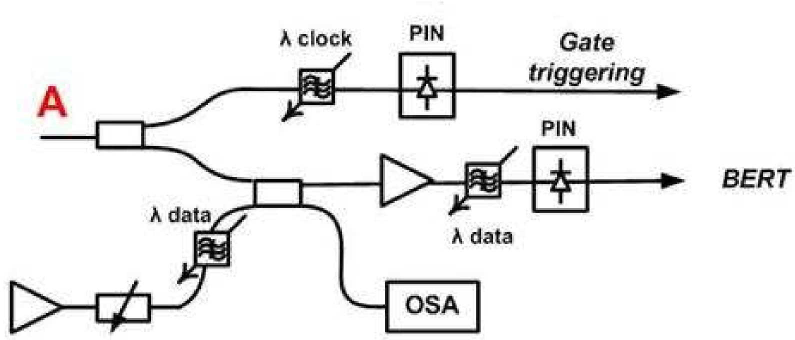

Figure 7. Receiver setup

The performance of the transmitted signals was estimated through BER measurements. Figure 8 depicts the BER curves after each loop for the case of OOK modulation at the rate of 22-Gb/s. The BER curves were derived through OSNR degradation at the receiver side.

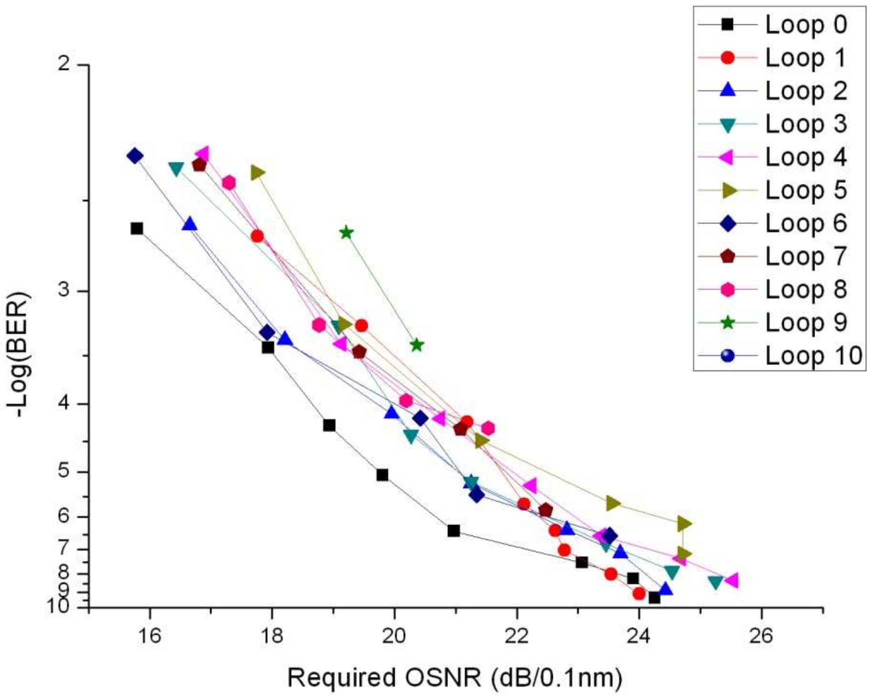

Figure 8. BER curves for OOK data after each loop at 22-Gb/s

Figure 9 illustrates the eye-diagrams of the OOK transmitted signal after a number of loops. As the screens show, the impairments that derived through the loop circulations result in the amplitude degradation of the optical signal (eye closure) as also in the increase of the time jitter.

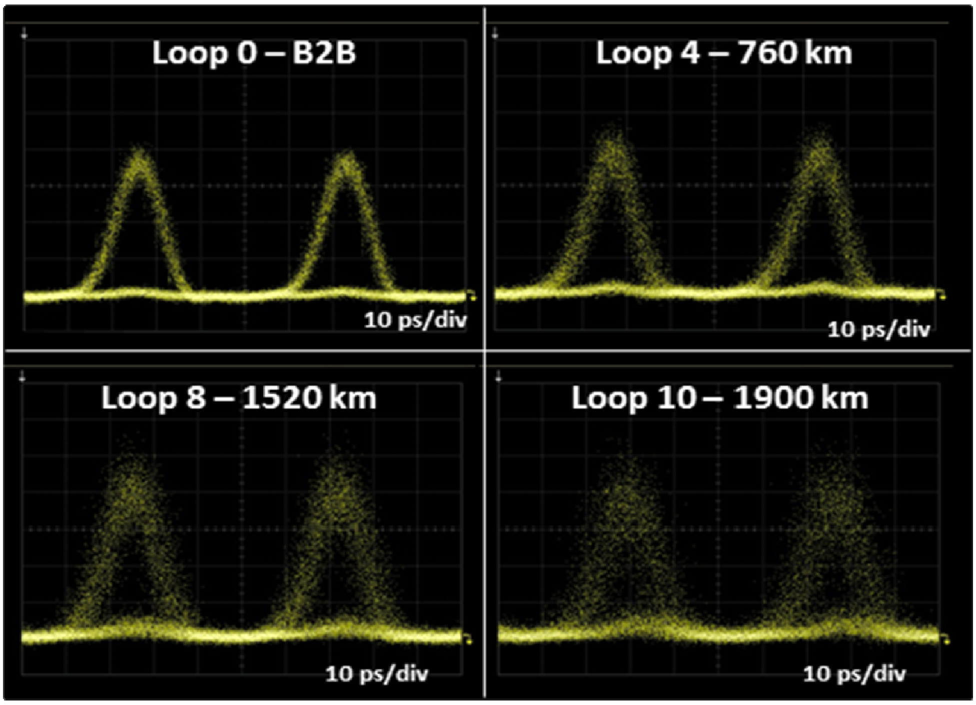

Figure 9. Eye-diagrams of OOK modulated signal at 22-Gb/s after loop circulations

Finally, Figure 10 shows the eye-diagrams of the transmitted 22 GHz DPSK modulated signal over the same optical link. The better performance, as depicted in the screens, is due to the better dispersion tolerance of DPSK signals and the use of balanced detection.

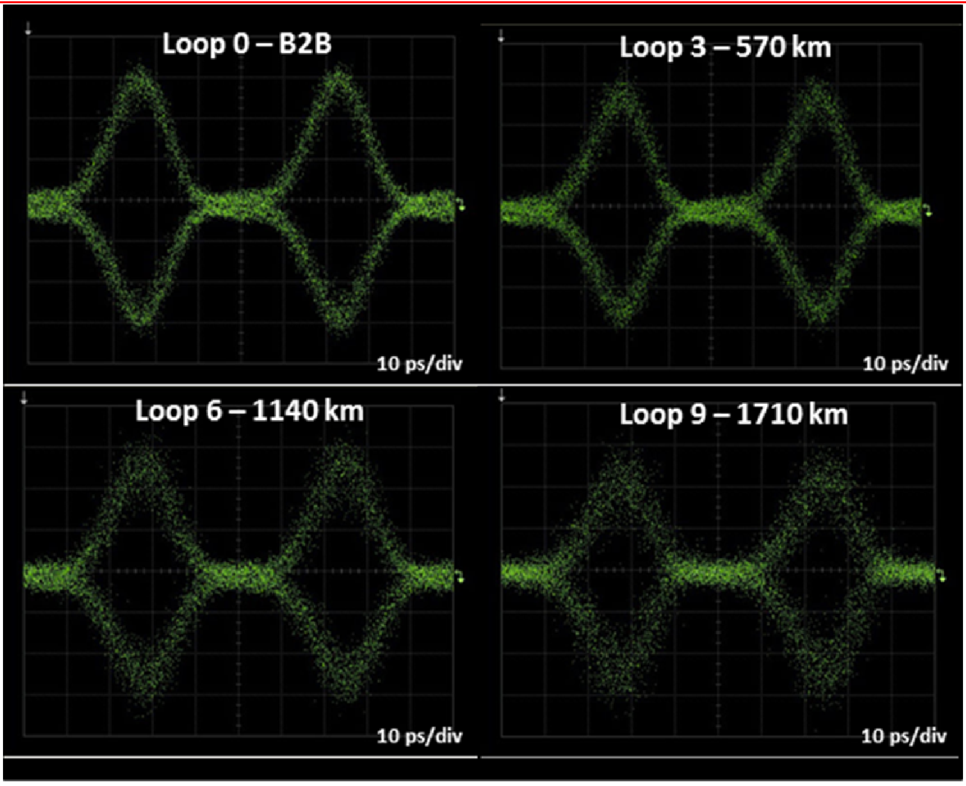

Figure 10. Eye-diagrams of DPSK modulated signal at 22-Gb/s after loop circulations

4.4 Benefits of Digital Backpropagation in Coherent QPSK and 16QAM Fibre Links (HWDU, UCL)

4.4.1 Introduction

Higher-order modulation formats have recently attracted much interest since they allow increased spectral efficiency and, therefore, higher capacity optical transmission systems without the requirement for installing new fibre. Coherent detection is a particularly effective approach to receive such formats as it provides access to the full information (amplitude and phase) on the optical field, in both polarisations, enabling powerful DSP algorithms to compensate for linear and nonlinear impairments.

In the section presented below we extend the initial work on the comparison of transmission performance of WDM systems at different symbol-rates [13], by estimating the potential benefit of digital backpropagation with optimum step-size. Polarisation-multiplexed, differentially-encoded quaternary-phase shift-keying (QPSK) and 16-quadrature amplitude modulation (16QAM) transmission on standard single mode fibre (SSMF) are considered at symbol-rates ranging from 7 GBd up to 56 GBd with fixed information spectral density.

4.4.2 Simulation Setup

We simulated WDM transmission with a range of symbol-rates between 7 GBd and 56 GBd simultaneously varying the channel-spacing between 12.5 GHz and 100 GHz to maintain a constant spectral efficiency of 2 bit/s/Hz in the case of QPSK and 4 bit/s/Hz for 16QAM. The number of channels increases when reducing channel spacing and symbol-rate from 72 channels at 7 GBd over 36 and 18 channels down to 9 channels at 56 GBd. Each WDM-channel was polarisation-multiplexed with decorrelated symbol-patterns and carried 215 symbols.

QPSK was generated by an IQ-modulator, modulating in-phase and quadrature of the optical field with a binary signal; in the case of 16QAM the modulator was fed with a 4-level driving signal, leading to 16 constellation points. The limited transmitter bandwidth was emulated in every case with a 5th- order electrical Bessel filter with a 3dB bandwidth of 0.8 x symbol-rate and the laser linewidth of the transmitter was set to 100 kHz.

The reference transmission system consisted of 13 x 80km SSMF spans, without any inline dispersion compensation. Erbium-doped-fibre- amplifiers (EDFAs) with a noise figure of 4.5dB were used to compensate for the optical fibre loss. These EDFAs were set to operate in saturation with a fixed output power of 17dBm; attenuators were used to obtain the required power levels. Table 2 summarizes the link parameters used throughout the simulations.

Table 2

α [dB/km]	0.2	D [ps/km/nm]	16	γ [1/W/km]	1.2
Span length	80	S [ps/km/nm^2]	0.06	PMD coefficient	0.1

At the receiver, the signal was detected with a single-ended coherent receiver. The linewidth of the LO-laser was set to be 100 kHz and the limited receiver bandwidth was also modelled with 5th-order Bessel filters, with a 3dB bandwidth of 0.8 x symbol-rate. The chromatic dispersion was compensated in the frequency domain and adaptive equalisers were implemented to compensate for PMD. While a standard constant modulus algorithm (CMA) equaliser could be used on QPSK [14], a radially-directed equaliser was implemented for 16QAM [15] to accommodate for the multiple intensity rings of this format. For the same reason, a decision directed phase locked loop (PLL) [15] was implemented to recover the carrier phase for 16QAM, while for QPSK the Viterbi & Viterbi algorithm [16] was used. After differential decoding, which has been applied to avoid burst errors due to phase ambiguity, Monte-Carlo error counting was performed to determine the BER.

Digital backpropagation (BP) was implemented for the central channel as a symmetric split-step algorithm (Wiener-Hammerstein-scheme [17]) with optimized step-size for every symbol-rate (25, 7, 1 and 1 step per span for 56, 28, 14 and 7GBd).

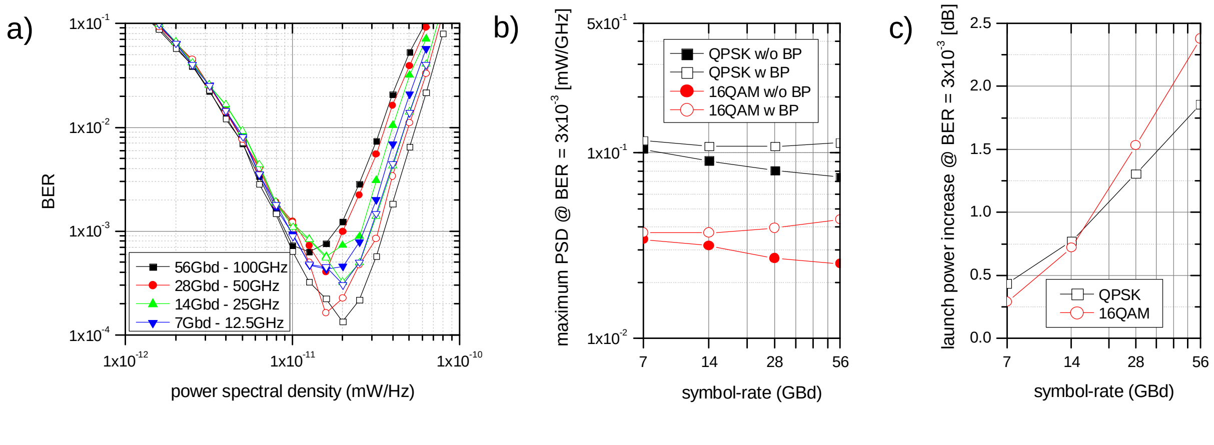

Figure 11 a) BER versus power spectral density for 16QAM with (open symbols) and without digital backpropagation (filled symbols) over 1040km link. b) The maximum PSD at BER=3x10-3 for QPSK as well as 16QAM and c) equivalent increase in launch power allowed by digital backpropagation vs symbol-rate.

4.4.3 Transmission results

In this work, the power spectral density (PSD), which is obtained by normalizing the launch power per channel to the channel spacing, was used as a metric for comparing transmission performance at different symbol-rates. When plotting it against the BER (see 16QAM results in Figure 11 a)), curves with the same spectral efficiency and modulation format overlap in the linear region of transmission, since the in-band noise power scales linearly with the symbol-rate, giving the same BER at the same OSNR, when the noise-power is integrated over the channel spacing. The use of PSD, rather than power per channel, thus, allows a direct comparison of nonlinear performance at different symbol-rates to be made. For both modulation formats nonlinear performance improves with decreasing symbol-rate, with 7GBd allowing a 3.1x10-2mW/GHz higher PSD at BER=3x10-3 than 56GBd (Figure 11 b)) for QPSK and 0.9x10-2mW/GHz for 16QAM. We attribute this behaviour to a reduced pulse overlap resulting in less intra-channel nonlinearities. This effect dominates the performance in the nonlinear transmission regime investigated here, as opposed to reduced walk-off effects which are due to a denser channel spacing.

Figure 11 b) shows that digital backpropagation is particularly effective when compensating channels with a higher symbol-rate, which is intuitively clear since signals with a higher bandwidth are subject to more severe nonlinear distortions and a larger proportion of the overall spectrum is backpropagated. Translating the results into the increase in launch power which can be achieved with digital backpropagation (see Figure 11 c)), we can conclude that this benefit amounts to 1.5dB in the case of QPSK and 2.1dB for 16QAM (comparing 7GBd to 56GBd). 16QAM is shown to benefit more from BP than QPSK (0.5dB at 56GBd), which we attribute to additional intra-channel nonlinearity due to several intensity levels which can be effectively compensated for by digital backpropagation.

4.4.4 Conclusions

In this work we investigated the benefit of digital backpropagation in WDM-transmission system employing PDM-QPSK or PDM-16QAM. We considered a wide range of symbol-rates and an uncompensated transmission link consisting of 1040km standard single-mode fiber. Similar performance improvement for both modulation formats was observed at 7GBd and 14GBd, while 16QAM outperforms QPSK by 0.2dB at 28GBd and 0.5dB at 56GBd. 16QAM is more heavily impaired by intra-channel nonlinearity due to several intensity levels, which leads in turn to a higher benefit when compensating for these effects. However, at lower symbol-rates the transmission behaviour is dominated by nonlinear crosstalk from adjacent channels, which can’t be compensated for.

4.5 Investigation of the role of Prechirp in Phase and Intensity Modulated Optical Transmission Dispersion Management Systems (FUB)

This contribution theoretically investigates the role of the prechirp in the chromatic dispersion compensation for high bit rate transmission systems based on phase and intensity modulation. A comparison between 100 Gb/s RZ DQPSK, DPSK and IM-DD formats is reported for long links encompassing G.652 fibre.

4.5.1 Introduction

The wider and wider bandwidth required from the users stimulates an increase in the transmission bit rate for long haul optical fibre systems and one of the aims currently is channel transmission at 100 Gb/s. To reach such capacities several technological approaches are required both in terms of advanced modulation formats and methods to mitigate the impairments due to the in-line degradation effects as the ASE of optical amplifiers and the dispersive and nonlinear fibre effects. Concerning advanced transmission and detection formats the combination of amplitude and phase modulation allows us to use higher bit-rate reducing the signal bandwidth. In particular, DQPSK is assumed as one of the most interesting techniques, since two symbols can be transmitted within one bit slot, consequently offering an enormous advantage in terms of mitigation dispersive impairments. On the other hand in long fibre links dispersive and nonlinear effects have to be controlled to reduce their disturbs in the propagation of wide signal bandwidth; the chromatic dispersion reduces the nonlinear Kerr impairments and therefore the use of a locally high chromatic dispersion can strongly limit especially the FWM effects in WDM systems. The accumulation of chromatic dispersion can be avoided by the use of compensating devices, such as fibre gratings or dispersion compensation fibres. Several works have showed that the periodic chromatic dispersion compensation, also known as dispersion management is the method that also limits the accumulation of self-phase modulation effects; furthermore several works, supported also by analytical explanations [18, 19], have shown that in IM-DD systems the introduction of a small value of chromatic dispersion at link input can further improve the transmission performance. However at our knowledge nobody has deeply investigated the advantages of the prechirp for transmission techniques based on phase modulation formats. The aim of this contribution is to investigate dispersion management systems based on the phase modulation with and without prechirp. We first report a brief analytical investigation and subsequently a numerical analysis on RZ-DPSK and RZ-DQPSK formats compared with IM-DD systems for 40 and 100 Gb/s bit rates in long G.652 links. Our results clearly show that the prechirp does not offer any advantage in case of random modulation in the phase plane (as in the DQPSK case), while it has a clear success when the phase changes in two antimodal points as in the DPSK case. However the advantages of DQPSK are much more evident with respect to DPSK (and IM-DD) systems due to its narrower bandwidth.

4.5.2 Simulation tool

This investigation is based on a numerical analysis carried out by means of a simulation code, based on MATLAB language and which was originally tested in the framework of the IST ATLAS.

The transmission line is supposed to be composed by G.652 fibres, simulated by means of the split-step method, fibre gratings, that periodically compensate the fibre chromatic dispersion, and optical EDFA amplifiers, assumed to have a flat gain, that add ASE noise.

Three modulation schemes were investigated: an IM-DD system, a RZ-DPSK and a RZ-DQPSK.

This numerical investigation is carried out on the same kind of dispersion management link that was deeply investigated in [18, 20] for a 40 Gb/s IM-DD system with Gaussian pulses having a FWHM duration equal to 5 ps. The fiber parameters are: α=0.25 dB/km, D=16 ps/nm/km, D_3=0.06 ps/nm^2/km, γ=1.3 (Wkm)$^{-1}$; the fiber grating α_T=1.5 dB, D_T= -1600 ps/nm, D_{T3}= -6 ps/nm^2, γ=0 and the EDFA G=26.5 dB, L_{amp}=100 km, F=6 dB.

4.5.3 Theory

In this short description we will try to simply illustrate the nonlinear behaviour in the pulse propagation in links with dispersion management for different modulation formats.

If the transmitted pulses are so short that the spacing between dispersion compensating stations greatly exceeds the dispersion length, a large number of pulses belonging to the same channel overlap during propagation and their nonlinear interaction leads to transmission impairments. When all transmitted pulses are in-phase, each overlapping pulse contributes to the total nonlinear distortion with an in-phase and an out-of-phase component. The in-phase component affects the pulse shape more than the out-of-phase component because it adds linearly to the pulses intensity, whereas the out-of-phase component adds quadratically. If the dispersion profile in the span between dispersion compensating stations is carefully designed, the in-phase component of the nonlinear distortion added in the first half of the span is exactly compensated by an opposite amount of distortion in the second half, therefore reducing the total in-phase component to zero [20]. In the ideal case in which the line loss is compensated for by an equal amount of distributed gain, this symmetric condition is achieved when dispersion compensation is equally split between the beginning and the end of the span [21]. This effect is clearly shown in Figure 12 where we report the points corresponding to the electrical field (real and imaginary part) of each pulse of a DPSK signal (512 pulses) after 700 km of the link in the absence of loss for an input peak power of 0.02 W, without prechirp in the left, and with prechirp on the right. The squeezing effect due to the prechirp allows us to well distinguish between “-1” and “1”.

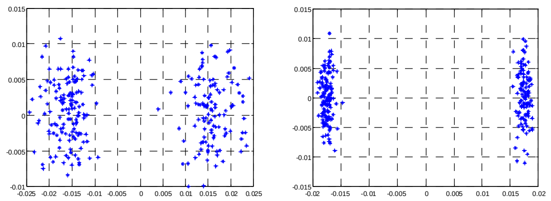

Figure 12: Field of each pulse of a DPSK signal after 700 km of the link in the absence of loss for an input peak power of 0.02 W, without prechirp in the left, with prechirp on the right.

When lumped Erbium amplifiers are used, the amount of pre-compensation that reduces the in-phase component to zero is smaller, because pulse attenuation leads the final part of the span to contribute less than the initial to the nonlinear interaction [22]. These results have been used in recent years as guiding rules for a careful optimization of the dispersion profile in high bit-rate links based on intensity modulation.

While the above results were originally derived for intensity modulation only, they apply to antipodal DPSK as well. With this modulation scheme, the pulses are either in-phase or out-of phase. Being the nonlinear interaction phase independent, it is possible to show that the qualitative picture that we have given above does not change. Therefore, the dispersion profiles that reduce the nonlinear impairments to a minimum in system based on intensity modulation will reduce to a minimum the nonlinear impairments in systems based on DPSK as well.

Looking at Figure 12 we immediately understand that the scenario is different with DQPSK systems. In fact, in this case, the nonlinear interaction takes place between pulses whose relative phases are multiple of 90 degrees, and the squeezing effect of Figure 12 cannot help to distinguish the four levels. Therefore there is no benefit in adjusting the pre-dispersion of the line to maximize the link capacity. The nonlinear impairments of DQPSK are therefore higher than the nonlinear impairments of DPSK, because there is no way to eliminate the in-phase component of the nonlinear distortion by acting on dispersion profile.

This fact, while explaining the generally recognized property that DQPSK is more prone to nonlinear impairments than DPSK, does not imply that the capacity of DQPSK systems is lower than that of DPSK systems. Nonlinear impairments lead to an amplitude jitter on the detected eyes that, with a large number of interacting pulses, may be approximated with a Gaussian noise. This extra noise produces a logarithmic decrease of the capacity with the variance of the jitter, according to Shannon's celebrated capacity formula. At the same time, however, the number of signal degrees of freedom of DQPSK is double than DPSK. The proportional doubling of the linear channel capacity more than compensates for the logarithmic decrease caused by the higher nonlinear noise, thus making the capacity of DQPSK systems generally higher than the corresponding capacity of DPSK systems also in the presence of nonlinear impairments.

These affirmations will be confirmed in the following by means of numerical simulations for different optical high bit rate transmission systems.

4.5.4 Results: prechirp effect on IM-DD, DPSK and DQPSK

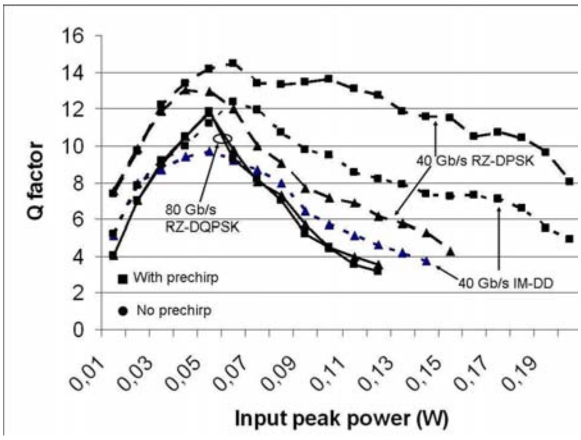

Figure 13: Q factor versus input power for 40 Gb/s IM-DD, 40 Gb/s DPSK and 80 Gb/s DQPSK.

To see the effect of the prechirp on the modulation formats in Figure 13 we report the Q factor vs input power for a link 700 km long for 40 Gb/s IM-DD, 40 Gb/s RZ-DPSK and 80 Gb/s DQPSK with and without prechirp of 78 ps/nm/km. All the three systems have the same symbol time equal to 25 ps and pulse duration equal to 5 ps. As reported in Figure 13 the improving effect of prechirp is much evident for IM-DD and DPSK, while its use for DQPSK is null, as foreseen from the reported theory.

The figure also shows that DPSK manifest advantages with respect to IM-DD in terms of performance that can be simply explained by the absence of jitter effect for the presence of a pulse in each time slot. Conversely DQPSK allows us to double the capacity in the same link conditions.

4.5.5 Results: comparison at 100 Gb/s

Figure 13 already shows the importance of RZ-DQPSK for 100 Gb/s long transmission systems. Furthermore to operate at such bit rate the time duration of pulse for IM-DD and

DPSK mus be reduced. We investigate on 100 Gb/s IM-DD, RZ-DPSK and DQPSK both in absence and in the presence of prechirp, looking also for the best pulse duration.

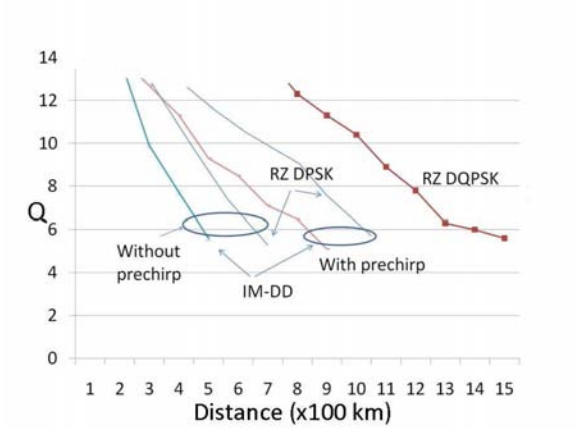

Figure 14: Maximum Q factor for 100 Gb/s IM-DD, RZ-DPSK and RZ-DQPSK.

In Figure 14 we report a comparison among IM-DD, RZ-DPSK and RZ-DQPSK in terms of maximum Q factor for an input power equal to 42 mW for different distances. In the IM-DD and RZ-DPSK cases the presence of the prechirp always induces benefit. Conversely for DQPSK, also if the prechirp does not help in performance improvement, permits to reach much longer distances.

To conclude this investigation we also report in Figure 15 the maximum transmission for WDM-DQPSK systems.

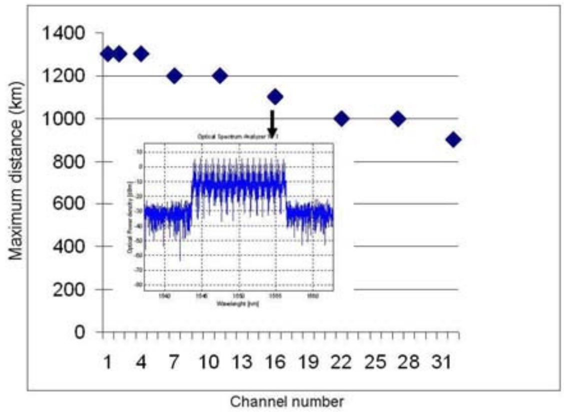

Figure 15: maximum propagation distance for nx100 Gb/s RZ DQPSK systems.

4.5.6 Conclusions

In this work we have reported a comparison of the effect of prechirp in dispersion managed links in different modulation formats. We show that prechirp induces benefits when the information is carried on binary formats as IM-DD and DPSK, while no effect is manifested in DQPSK, even though the advantages of DQPSK are wide with respect to the others even without the contribution of prechirp.

5. Signal regeneration (ORC, UoA, USWAN)

5.1 Optical regeneration based on phase-sensitive amplification (UoA)

5.1.1 Introduction

The first part involves UoA work on phase sensitive amplification. This work was carried out numerically and aimed at proposing a regenerator suitable for phase modulated signals in order to minimize the noise fluctuations without requiring a demanding phase locking technique prior the phase sensitive interaction. Although PSA has the ability to perfectly squeeze the noise impairing the phase, its practical implementation is very challenging and has to take care of the precise locking of the frequencies and phases of the interacting waves in advance. The regeneration experiments of [23] provided the proof of principle of amplitude and phase regeneration in interferometric and four-wave mixing (FWM) based PSAs, but are far from being practical solutions, because the pump and the signal originated from the same laser and the phase modulation was applied after the phase locking process. Only very recently, a phase sensitive amplifier utilizing injection locking and FWM was successfully demonstrated as the first black box regenerator based on a degenerate PSA [24]. The regenerator presented in [24] is mostly suitable for non-return to zero (NRZ)-DPSK signals as the locking process is based on injection locking a local laser with a constant envelope signal. UoA worked on a return-to-zero (RZ)-DPSK regenerator scheme (Figure 16) based on a non-degenerate PSA. The proposed scheme embodies two novel approaches in comparison with the up to date reported PSA techniques. It relies on the non-degenerate FWM based phase sensitive amplification which has the potential to offer multi-wavelength amplification and it eliminates the need for precise frequency and phase locking with the input signal. The conceptual scheme is plotted in the next figure.

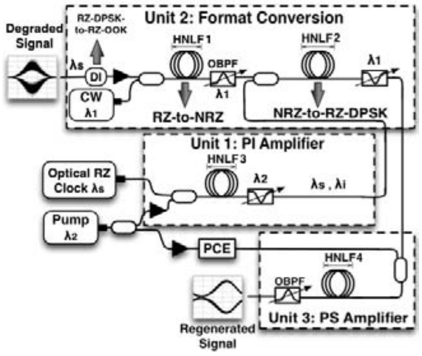

Figure 16: Block diagram of the all-optical DPSK regenerator. DI: Delay Interferometer, OBPF: Optical Band-Pass Filter, PCE: Phase Control Element.

5.1.2 Principle of operation and results

The scheme consists of three different units (Figure 16). The first unit prepares an auxiliary signal and an idler through a typical single-pump FWM process in a highly nonlinear fiber (HNLF). The auxiliary signal of the FWM process is a typical clock of Gaussian pulses (the typical amplitude pattern of RZ-DPSK signals) with repetition rate equal to the bit-rate of the degraded input. By using the first FWM module, we obtain three frequency- and phase locked waves whereas signal and idler are two identical RZ clocks. The data of the input RZ-DPSK signal must be loaded on the phase of both auxiliary signal and idler with the same polarity. The latter is a prerequisite in order for both signal and idler to experience phase sensitive amplification accompanied with phase noise squeezing as it will explained later.

The second unit undertakes the input signal data transfer onto the phase of the auxiliary signal and its idler. Initially, the second unit of the regenerator carries out the conversion of the signal phase information to amplitude. The incoming RZ-DPSK signal (λs) passes through a delay interferometer (DI) which demodulates it to a return RZ-OOK bit stream. The next step includes the conversion of the RZ-OOK to a non-return to zero (NRZ) bit sequence as the typical RZ-DPSK modulation format encloses NRZ phase modulation pattern. This step is accomplished with the use of a second XPM stage where the RZ-OOK bit stream is combined with a continuous wave (λ1). The RZ phase modulation transferred to λ1 leads to red and blue shifts of the frequency of the CW. This wave is then filtered with a narrow bandwidth optical bandpass filter centred at its wavelength which converts the CW to NRZ pulses. The NRZ bit stream is an inversed replica of the RZ-OOK stream [25]. At the final step, the NRZ-OOK copy of the input signal, the auxiliary signal and the idler are coupled into a second XPM module (HNLF) in order to complete the transfer of the NRZ pulses to the phase of the RZ clocks. The power of the NRZ-OOK bit stream must be properly adjusted -taking into account the nonlinear medium parameters- in order to obtain a phase difference equal to π between the two phase states of the auxiliary signal and its corresponding idler. After this process, auxiliary signal and idler are transformed to two identical, phase and frequency locked RZ-DPSK waveforms.

The third unit embodies the phase sensitive amplification of the two RZ-DPSK waves. The carriers of the auxiliary signal, the idler and the pump are in advance locked (unit 1 task). A piezoelectric transducer could play the role of a dynamic phase controller in a typical experiment [24]. At gain maxima, both RZ-DPSK waveforms will exhibit a significant reduction of the phase noise and wide-open final RZ-DPSK eye diagrams. The phase noise squeezing capability of the PSA is dependent on the gain properties. The experiments of [23] and [24] have shown that PSA gain ratios greater than 15 dB are sufficient in order to provide the quantization of the output phase noise. The device could be exploited in a threefold manner working either as an in line amplifier-regenerator or a pre-amplifier at the detection level (the output is the auxiliary signal) or even as a wavelength converter-regenerator (the output is the regenerated idler).

The nonlinear medium in this work is a typical HNLF. The HNLF transmission is simulated by numerically solving the nonlinear Schrödinger equation (NLSE) with the use of the split-step Fourier (SSF) method. The model accounts for up to the fourth-order dispersion. Moreover, in order to encounter the phase noise of all the waves participating in the scheme, and to highlight the independence of the proposed scheme on the input signal phase and frequency, rate equation model for the simulation of semiconductor lasers has been utilized. Typical arbitrary semiconductor lasers with linewidth equal to 500 kHz and relative intensity noise of -140 dB/Hz are considered. The auxiliary signal is a train of Gaussian pulses with pulsewidth equal to 6.25ps and repetition rate equal to 40GHz. The wavelengths of pump (λ_2), CW (λ_1) and signal (λ_s) are chosen to be equal to 1556 nm, 1525 nm and 1536 nm respectively. For the RZ to NRZ optical conversion, a 1 km long HNLF (HNLF1) with nonlinear parameter γ=12W^{-1}km^{-1}, fiber losses α=0.7dB/km, zero dispersion wavelength λ_0=1540nm and dispersion slope dD/dλ=0.03ps/nm^2/km was considered. Unit1 and unit3 of the scheme rely on a 500m long HNLF (HNLF3, HNLF4) with λ_0=1555nm. The pump power in each stage is equal to 27dBm providing small signal gain equal to 18dB and 24dB for the unit1 and the unit3 respectively. The fiber considered for the NRZ-OOK to RZ-DPSK conversion is 350m long (HNLF2) with λ_0=1555nm. The EDFAs are modeled as constant gain amplifiers that induce additive Gaussian noise with noise figure equal to 5dB. Each EDFA is accompanied by an optical bandpass Gaussian filter with 160 GHz 3dB bandwidth. The output of the DI is amplified to 26.9dBm and coupled with a 25.72 dBm CW for the RZ to NRZ conversion. At the output of the format conversion unit the CW is filtered by a bandpass optical filter with 40 GHz 3dB bandwidth.

The distortion of the amplitude and phase characteristics of the RZ-DPSK input was carried out by simulating its fiber transmission through an 800km long transmission link. The link consists of typical single-mode fibers (L_{SMF}=40km, α_{SMF}=0.22dB/km, γ_{SMF}=1.3W^{-1}km^{-1}, β_2=-20ps^2/km) and dispersion compensating fibers (L_{DCF}=40km, α_{DCF}=0.27dB/km, γ_{DCF}=4.5W^{-1}km^{-1}, β_2=20ps^2/km) and optical amplifiers with noise figure equal to 5dB which are placed periodically every 80km. The mean power of the RZ-DPSK signal at the input of the link was 0dBm. Figure 17 (a) shows the original output of the DI (RZ-DPSK to RZ-OOK conversion) which shows the noise impaired signal and Figure 17 (b) shows the result of the RZ to NRZ conversion. The subsequent eye diagram in Figure 17 (c) corresponds to the phase content of the auxiliary signal after the XPM interaction between the signal, the idler and the NRZ replica of the input RZ-DPSK. The power of the NRZ (mean power equal to 22.7dBm) and the fiber length and nonlinearity (350m, 12W^{-1}km^{-1}) are properly selected so as to convert the NRZ amplitude modulation into a NRZ phase modulation with modulation depth equal to π, through the XPM process. The eye-diagram of Figure 17 (d) is the phase content of the auxiliary signal after the PSA process. Eye diagrams and histograms in Figure 18 for a heavily impaired signal show the remarkable noise squeezing performance of the saturated PSA.

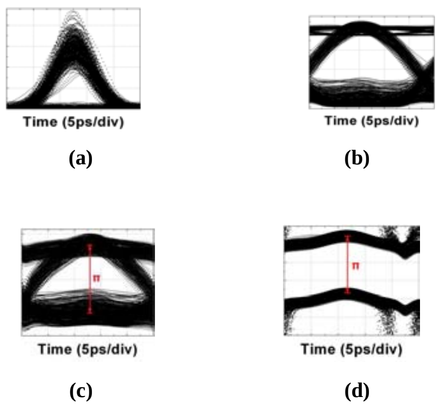

Figure 17: Eye diagrams of the RZ-OOK signal after DI (a), NRZ after format conversion at unit 2 (b), auxiliary signal phase before regeneration (c) and after regeneration (d).

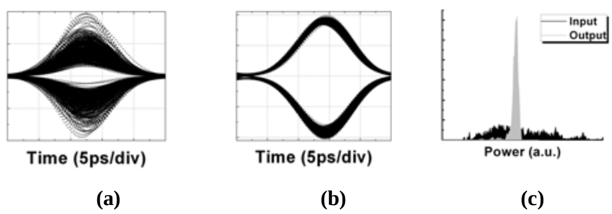

Figure 18: Eye diagrams before (a), after regeneration (b) and corresponding histograms (c).

5.2 Amplitude regeneration of phase modulated signals (UoA)

5.2.1 Introduction

During the third year, UoA focused on the potential for limiting amplification of constant envelope signals with the use of simple semiconductor lasers. A very efficient way to reduce the non-linear phase noise is to suppress the amplitude noise of the degraded phase modulated signal somewhere in the middle of the transmission link or in a periodic manner. Amplitude limiters based on Non-Linear Amplifying Loop Mirror (NALM) [26], and on saturated four wave mixing (FWM) [27] in highly nonlinear optical fibers are the most prominent schemes. Both techniques have been proven to exhibit significant noise suppression features, however their use in a commercial transmission system is still not attractive due to their increased size and the need for extra components such as optical amplifiers and optical filters. During this period UoA studied an alternative amplitude limiter based on optical injection locking in a discrete mode semiconductor laser [25] that offers enhanced amplitude noise squeezing, implementation simplicity and ability to reproduce the phase modulation bandwidth of the incoming signal up to multi GHz bandwidth, thus enabling the amplitude regeneration of constant envelope phase encoded signals. The experiment demonstrates the regeneration principle for 10 Gb/s differential PSK (DPSK) signals. The technique could be extended for M-PSK signals as well.

5.2.2 Experimental setup and results

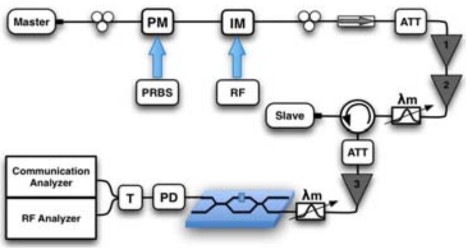

Figure 19: Block diagram of the experimental set-up. PM: Phase Modulator, IM: Intensity Modulator, PRBS: Pseudo Random Binary Sequence, RF: Radio Frequency Wave Generator, EDFA1: OSNR Controller, EDFA2: Injection Level Controller, EDFA3: Receiver Amplifier, PD: Photodiode and T: RF Splitter.

The scheme is tested for 10Gb/s PSK signals, meaning that the slave laser current must be tuned at values which reassure that its intrinsic modulation bandwidth is of the same order. The second parameter that determines the locking bandwidth is the power of the master injected into the slave. The injection level must be properly adjusted so as to enable the reproduction of master phase modulation at the slave with the minimum transfer of its amplitude noise properties. The block diagram of the experimental set-up is depicted in Figure 19. A tunable external cavity laser is used as the master laser and is phase modulated at 10 Gb/s with the use of a phase modulator and a pseudo random binary sequence (PRBS) generator. The bit sequence is a 2^{31}-1 one. The polarization controller before the phase modulator is used in order to align the laser with the phase modulation axis of the modulator. The variable attenuator before the first erbium doped fiber amplifier (EDFA) controls the optical signal to noise ratio (OSNR) of the transmitted PSK signal while the second EDFA controls the injection level of the signal that is injected into the slave laser. The output of the second EDFA is filtered in order to remove amplified spontaneous emission noise (ASE) with the use of a band-pass filter of 1nm bandwidth and then is fed into the slave laser via a circulator. The single mode slave laser exhibits 10Gb/s modulation bandwidth at currents close to 98mA. The output of the slave laser is sent to a second variable attenuator and then amplified by a third EDFA which plays the role of the pre-amplifier before the receiver required for systematic bit-error rate (BER) measurements. The output of the master is also launched into the same amplifier in order to provide a fair comparison of the master and slave BER potential. Finally, both slave and master outputs are coupled into a 100 ps delay interferometer for the differential detection at a single 12 GHz bandwidth photodiode and monitored in a 20 GHz communication analyzer. The experimental study is carried out for two noise regimes. First, we investigate the performance of the regenerator as an inline amplitude limiter where ASE noise of the EDFA affects both amplitude and phase of the signal. Then we evaluate the regenerative characteristics of injection locking in a special case where the signal is only impaired by amplitude noise. This noise regime seems artificial; however noise only at the amplitude could appear at the output of a phase sensitive amplifier-regenerator (PSA) operating in the linear regime [23]. It is known, that a linear PSA squeezes perfectly the phase noise of phase-modulated signals, however the phase noise is converted to amplitude noise through the phase sensitive amplification process.

First we investigated the case where the master is degraded by ASE noise. For different noise levels of the master, we investigated the amplitude squeezing properties of the injection locked laser. The analysis includes BER measurements as a function of the signal OSNR and the receiver power. The results are promising as they reveal that the injection locked laser provides a significant power penalty improvement of 1.5dB (Figure 20, left diagram) and relaxes the required OSNR for a given BER by 1.5 dB as well. It must be noted that injection locking operates as an amplifier in these experiments. Its gain was measured to be close to 20dB.

In the second case, we considered severe noise degradation only at the intensity of the master trying to emulate the case where phase noise is removed by a linear phase sensitive regenerator. The experimental analysis that follows (Figure 21) shows that an injection locked semiconductor laser could comprise the ideal regenerator to handle intensity noise degraded phase encoded signals. To experimentally emulate the intensity noise case, we applied sinusoidal perturbation to the NRZ-DPSK signal with the use of an intensity modulator. The results show remarkable regenerative performance. Error free operation (BER < 10^{-9}) is recorded for the output of the slave (P_{rec}=-15dBm) whilst the master BER is limited to 10^{-5}. The eye-diagrams reveal the perfect squeezing of the amplitude perturbation after injection locking. It must be noted that similar squeezing performance was recorded for all frequencies from 1 to 10 GHz.

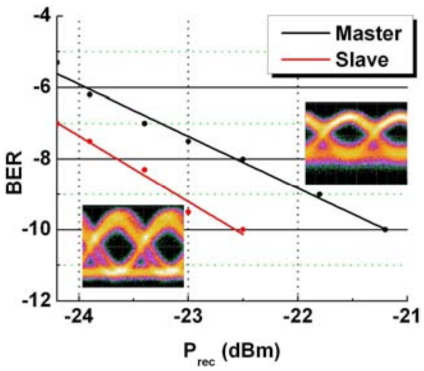

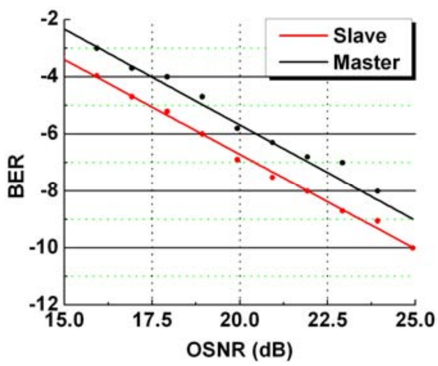

Figure 20: (Left diagram) BER measurement as a function of the receiver power for master OSNR equal to 30 dB. (Right diagram) BER is a function of the master OSNR keeping the received power equal to -7.5dBm.

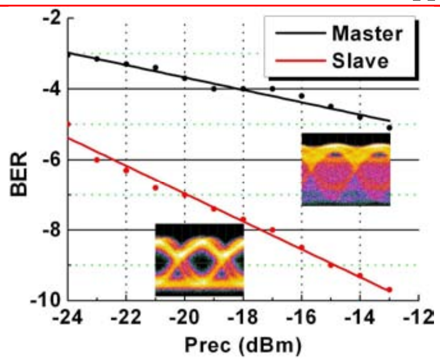

Figure 21: BER measurement as a function of the receiver power when the master is perturbed by a strong 1GHz sinusoidal signal, (master OSNR=30dB).

5.2.3 Conclusions and next steps

The results presented in Sections 5.1 and 5.2 showed the attractive properties of two diverse regenerators of coherent modulation formats, namely phase sensitive amplifiers and injection locked lasers and their complementary roles in handling phase noise and amplitude noise signals. Next step is the combination of both techniques so as to minimize the overall noise impairing the constant envelope signals.

5.3 Phase and Amplitude Regenerators for (Differential) Phase Shift Keying signals (ORC, UoA)

All-optical signal regeneration is an effective approach to eliminate accumulated signal impairments in high performance optical communication systems without the need of optical/electronic/optical (O/E/O) conversion. Until recently, the seemingly abundant fibre bandwidth has allowed engineers to follow the relatively simplistic approach of switching light on and off to encode the information to be transmitted, i.e. transmitting the information using On-Off Keying (OOK) modulation formats. However, the bandwidth demands are now such that this approach is no longer sustainable. Cutting edge research in optical transmission adopts techniques which have been originally developed for RF communications and involve manipulation of both the intensity and phase of the transmitted field. Advanced multilevel modulation formats, Multi Phase Shift Keying (MPSK) and approaches such as Differential Phase Shift Keying (DPSK), Differential Quadrature Phase Shift Keying (DQPSK) and Quadrature Amplitude Shift Keying (QAM), have emerged as an attractive vehicle for optical transmission. As well as offering high spectral efficiency, these approaches also offer considerable advantages in terms of optical signal to noise ratio and resilience to the various transmission impairments. However, the use of the complex optical-field gives rise to a new dominant limitation to system performance, namely nonlinear phase noise. Nonlinear phase noise arises from nonlinear interactions mainly due to Kerr nonlinearity [28, 29] and they depend on the amplitude and phase noise evolution of all signals transmitted within the fibre as many individual wavelength channels are usually transmitted simultaneously. Each channel is also degraded by other sources of amplitude/phase noise generated within the transmission line including amplified spontaneous emission from optical amplifiers and quantum noise, to name but two. A good regenerator should then be capable of suppressing the amplitude and phase noise of the signals to allow further transmission and to suppress the seed noise that causes nonlinear signal phase noise to build up in the first place.

As mentioned in the previous sections, most work on all-optical regeneration of DPSK signals to date has focused on the elimination of amplitude noise only, which can be achieved using cross-phase modulation (XPM) in a nonlinear amplifying loop mirror (NALM) [30] or using saturation of FWM interaction caused by pump depletion in a nonlinear fibre [31, 32]. A different approach to elimination of amplitude and phase noise simultaneously is to adopt some forms of phase-to-amplitude format conversion and then to apply amplitude regeneration on the amplitude encoded signal [33]. However, a simpler solution is to directly eliminate the phase noise.

Phase and amplitude regeneration can be achieved directly by exploiting the phase squeezing capability and the saturated regime of phase-sensitive amplifiers (PSAs). Contrary to a phase-insensitive amplifier, where the in-phase and quadrature components of the electric field of the signal experience the same gain, in a PSA the two quadrature components are amplified differently: the in-phase signal component experiences a gain g, while the quadrature component experiences a de-amplification 1/g, so that phase squeezing can be achieved.

Initial proof of concept results have recently been demonstrated by Croussore et al [34, 35, 36] in either single- or dual-pump configurations using either interferometric configurations based on nonlinear optical loop mirrors [34], or using FWM processes [35, 36] in fibre. However, due to the technological challenges to recover the carrier and phase-lock the newly generated pump(s) to the DPSK signal itself, their phase relationship was, so far, artificially guaranteed using a single (master) continuous wave (CW) laser [35, 36], making the regenerator impractical for use in a real transmission system. However, technologies move on and a FWM-based all-optical phase and amplitude regenerator set up in a “black-box” was recently proposed and experimentally demonstrated. The demonstration was based on a dual-pump degenerate PSA configuration and acted on a 40Gbit/s DPSK signal [24, 37]. In this Section these results are reported and discussed.

The experimental setup is shown in Figure 22. The data signal was a 40Gbit/s non-return-to-zero (NRZ)-DPSK, 2^{31}-1 pseudo-random bit sequence (PRBS). The effects of phase and amplitude noise were emulated by modulating the signal phase and amplitude using additional phase and amplitude modulators, driven sinusoidally at frequencies of ~20GHz and ~1GHz, respectively. The distorted signal was then launched into the black-box regenerator. Part of the signal was tapped off to facilitate the frequency and phase locking of the two local pumps used in the degenerate PSA configuration, as follows. The tapped signal and a

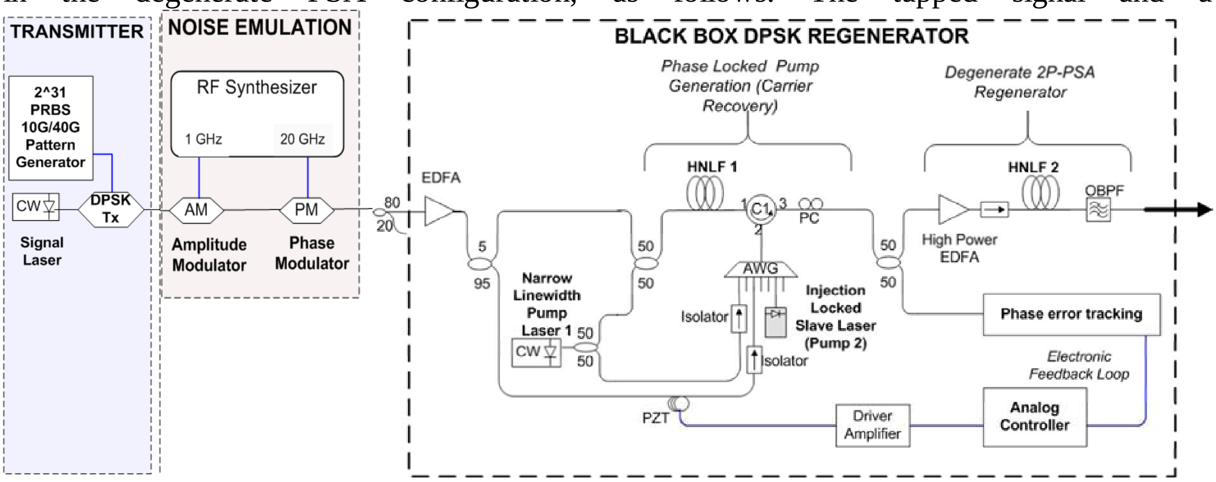

Figure 22: Experimental set-up of the 40Gbit/s phase and amplitude regenerator [24, 37].

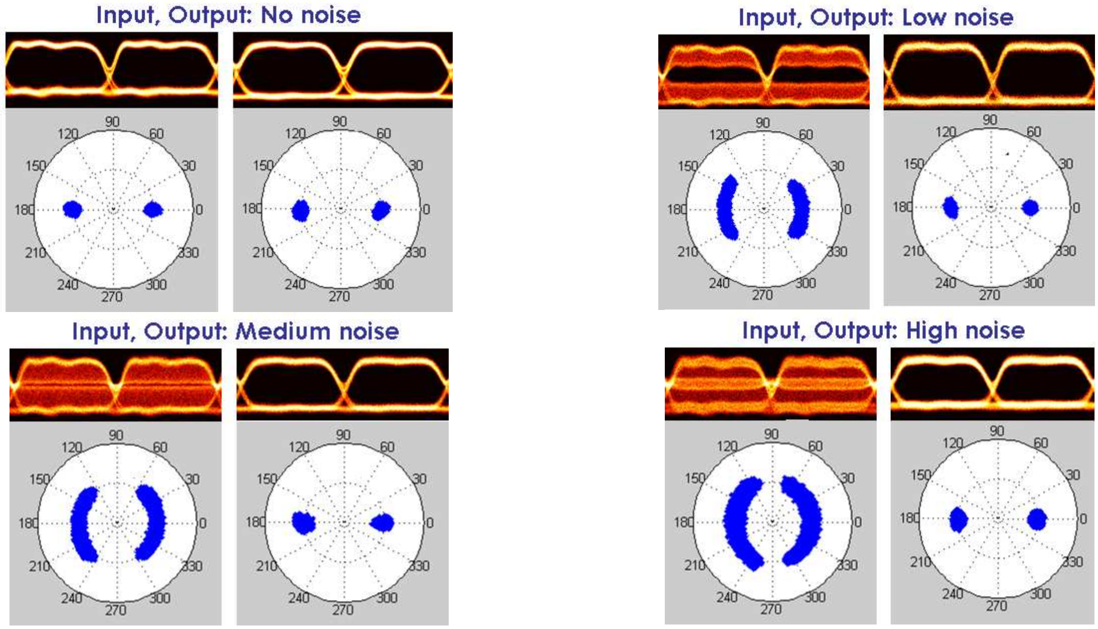

Figure 23: Demodulated eye diagrams after balanced detection and differential constellation diagrams (showing bit-to-bit phase changes) for different levels of phase noise only [24, 37].

narrow linewidth CW laser (Pump 1) detuned from the signal by 200 GHz were first combined in a germano-silicate highly nonlinear fibre (HNLF) (see Ref.[24] for the corresponding fibre parameters) to parametrically generate an idler wave that served as the seed for the second pump. Then, the weak idler wave was filtered and injected into a (slave) semiconductor laser to generate the second phase-locked pump (Pump 2) by means of a multiplexer [38]. As the injection locking is a much slower process than FWM, any high frequency fluctuations present on the original data signal were not transferred onto the output of the slave laser. Pump 1 and Pump 2 were then coupled together with the data signal, amplified up to ~34 dBm and launched into an alumino-silicate strained HNLF which was used for the PSA regeneration. This fibre exhibited an increased Stimulated Brillouin Scattering (SBS) threshold, which allowed its use without the need for any active SBS suppression scheme and the corresponding parameters are reported in [24]. The relative powers of the pumps and signal were adjusted for optimal regeneration performance. Any slow (sub kHz) relative phase drifts between the interacting waves picked up due to acoustic and thermal effects present prior to the PSA fibre were compensated for by an electrical phase-locked loop that controlled a piezoelectric-based fiber stretcher in the pump path.

The performance of the regenerator was first studied using a constellation analyzer based on a homodyne coherent receiver and offline digital signal processing (DSP) operating at 10Gbit/s [39, 40]. In this case, phase noise only (with the modulator driven at ~5GHz [24]) was added to the signal. From these measurements, amplitude and bit-to-bit phase changes were calculated and the corresponding DPSK constellation diagrams are shown in Figure 23, where it is shown that the phase noise can be squeezed by the regenerator to the back-to-back level and almost negligible amplitude noise is induced even for as extreme peak-to-peak values of phase distortion as ±80deg. Corresponding bit error ratio (BER) measurements (not shown here) confirmed error free operation with negligible power penalty as compared to the back-to-back even for the most extreme case of added noise reported in Figure 23.

The noise performance of the regenerator was also studied at 40Gbit/s using eye diagrams and BER measured for various levels of phase-only, amplitude-only and simultaneous amplitude/phase perturbations. The key results are summarized in Figure 24 showing results for phase-only perturbations for ±30 deg and ±50 deg (Figure 24 (a)), amplitude-only perturbations for ±25% and ±50% (Figure 24(b)) and amplitude and phase perturbations when the lower levels of amplitude and phase perturbations were then simultaneously applied (Figure 24(c)). Note that the higher levels of the amplitude and phase noise were chosen to be very close to the regenerator limit (over this limit the BER curves are no longer straight lines), as shown in Figure 24(b) (green triangles). The regenerator restores the BER performance to the back-to-back level even for relatively high levels of noise (with noise in the phase, amplitude, or both) that otherwise result in a BER power penalty of more than 10 dB (at a BER of 10-9), see Figure 24. In fact, the BER performance is actually improved for modest noise levels as compared to the back-to-back case, which we believe to be due to a slightly non-optimal transmitter configuration.

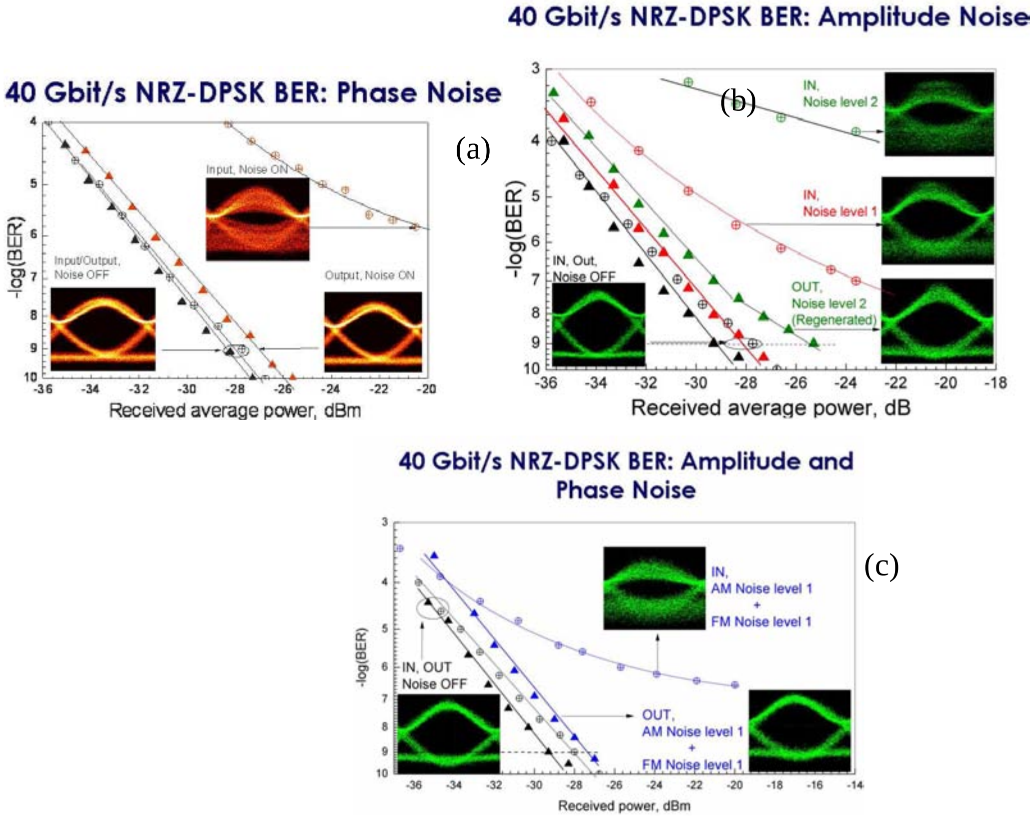

Figure 24: BER curves (measured using single-sided receiver detection after a 1-bit delay line interferometer) and corresponding eye diagrams (measured using a dual-port optical sampling oscilloscope after the 1-bit delay line interferometer) when phase-only (a), amplitude-only (b) and both amplitude and phase (c) noise is added at the input of the system. The performance at the regenerator input and output is shown as circles and triangles, respectively (no noise: black; lower level of amplitude or phase noise: red; higher level of amplitude or phase noise: green; combined (lower level) amplitude and phase noise: blue) [24, 37].

5.4 All-Optical QPSK Signal Regeneration in a Novel Multi-Format Phase Sensitive Amplifier (ORC, UoA)

As discussed in the previous section on “Phase and Amplitude Regenerators for (Differential) Phase Shift Keying signals”, the future of optical fiber communications will be dictated by the need for long reach, high capacity and energy efficient technologies. Transitioning to spectrally efficient modulation formats such as Quadrature Phase Shift Keying (QPSK) provides significant capacity gains in long haul optical links. Fully coherent optical signal detection combined with high speed analog-to-digital conversion allows signal processing in the electronic domain, providing capabilities such as compensation for chromatic and polarization mode dispersion, as well as for some of the accumulated nonlinear phase noise which is the dominant limitation in extending coherent transmission spans [41]. However, the power consumption as well as the significant computing overhead associated with the aforementioned electronic functions [42] means that a combination of optical signal processing with optical dispersion compensation may still prove competitive for long haul transmission, particularly as signalling rates continue to rise. All-optical signal regeneration techniques capable of processing advanced formats with multiple levels in phase or/and amplitude are, thus, very attractive. One proposed scheme utilizes a pair of conjugated signal-idler channels transmitted along the link and combined in a nondegenerate PSA [43]; however this wastes valuable transmission bandwidth, and requires impractically low levels of residual dispersion post–compensation. Other proposals to all-optically regenerate QPSK have focused on scaling schemes intended for use with binary level signals, including an indirect approach utilising format conversion to on-off-keying (OOK), OOK regeneration, and OOK to QPSK conversion [44] as well as a more direct technique using two parallel binary phase shift keying (BPSK) regenerators [45]. Such schemes are significantly complicated by the requirement to fully length-match and stabilise multiple optical paths, as well as a component count that increases appreciably with the density of the modulation format, potentially offsetting some of the economic benefits of the spectrally efficient formats. In this section we propose a novel concept using inline phase sensitive fiber optical parametric amplifiers to provide the direct all-optical regeneration of arbitrary multilevel phase encoded signals. We use it in the first demonstration to our knowledge of black-box all-optical QPSK phase regeneration (as in Figure 25).

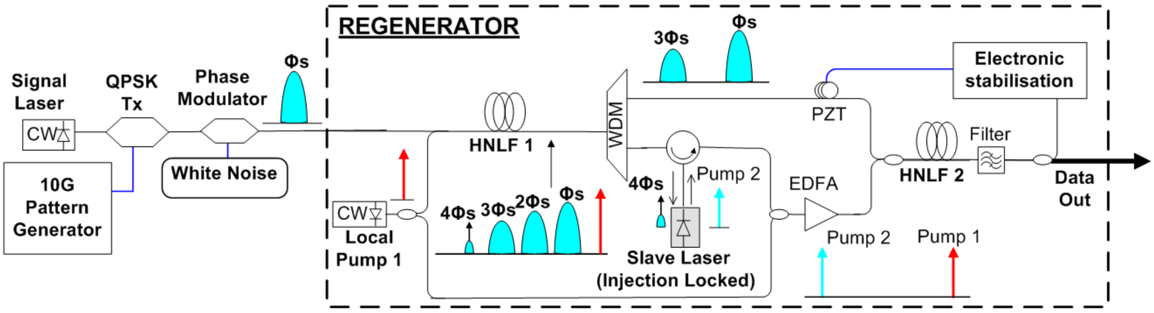

Figure 25: Experimental setup, PZT – piezo fiber stretcher, HNLF – highly nonlinear fiber, CW – continuous wave, QPSK Tx – QPSK transmitter.

Multi-level phase regeneration requires a staircase phase transfer function. For an M-level optical PSK signal, we propose to achieve this by interfering it with a conjugated (M-1)th phase harmonic. A semi-analytical way to understand this is as follows. If a QPSK signal is considered (M=4), a simple way to express this is:

$$\exp(A \times i \times f_{out}) = \exp(i \times f) + m \times \exp(-i \times 3f),$$

where f is the input signal modulation, f_{out} is the output modulation (regenerated), A is a phase-to-amplitude conversion term and m is a coefficient to optimise the phase regeneration.

Figure 26 (a) and (b) illustrate in a simple fashion how this provides phase regeneration. For symbols aligned to the principal axes of 0° and 90° (I and Q axes), f and $-3f$ are exactly in phase with each other, and their combination leads to constructive interference as shown in Figure 26 (a). However, for symbols aligned at 45°, f and $-3f$ are 180° out of phase leading to destructive interference. Figure 26 (b) shows an example of the phase re-alignment for two sample points with input phases of 30° and 80°.The value of m optimises the overall phase transfer characteristics; for a $\pi/2$ step period (i.e. a QPSK signal) it should be approximately 0.35-0.5 (in amplitude), as detailed numerical simulations also confirmed. The complete transfer function is shown in Figure 26 (c). To practically achieve multilevel phase regeneration, we utilize a two-step process. First, the QPSK signal is mixed with a pump to generate a four wave mixing (FWM) comb, including the required $3f$ (referred to from now on as the harmonic), see Figure 26 (d). The signal and harmonic are then combined inside a dual pump non-degenerate PSA where the coherent addition occurs. Of the two required pumps, the first is derived from the free running laser originally used in the comb generation stage, and the second by injection locking the $4f$ (modulation stripped) wave to a semiconductor laser, satisfying the phase locking requirement. The relative powers of the signal and harmonic need to be optimized to take the amplifier power gain, G, into account; as such a signal-harmonic offset of m_{eff} is used, where $m_{eff}=m$*sqrt(1-1/G). Reconfiguring the regenerator to an alternate modulation format such as 8-PSK can be achieved simply by generating a broader FWM comb (by increasing the signal and pump powers), passively selecting the desired harmonic and tuning the injection locked laser to the corresponding frequency.

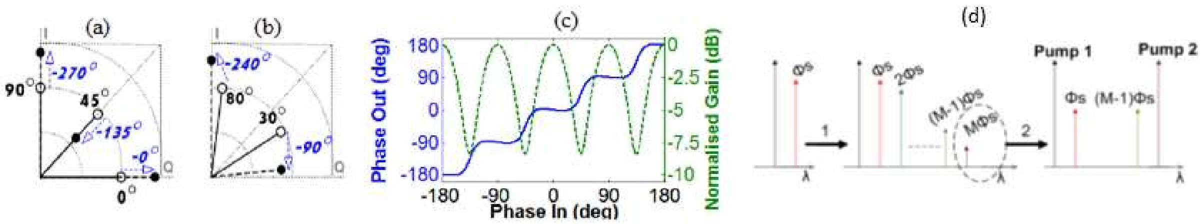

Figure 26: (a) Illustration of how amplification of I and Q quadratures is achieved while 45° component is de-amplified. White circles, input , dotted vector , black circles, output (b) Example with symbols at 30° and 80° (c) Complete semi-analytical transfer function showing phase and amplitude response. (d) Regeneration in two steps – 1) Nonlinear generation of phase harmonics via four wave mixing (FWM) followed by pump recovery, 2) Parametric phase sensitive gain.

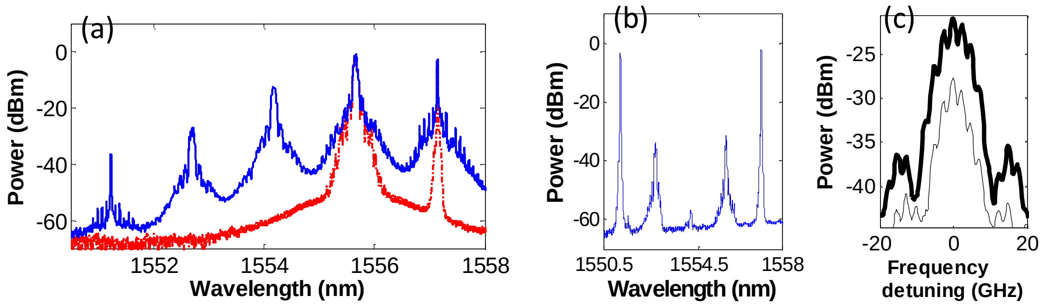

Figure 27: (a) FWM comb generation stage input (dotted) and output(solid). (b) HNLF2 input and (d) signal spectrum at HNLF2 output, thick line (top) is PS maximum, thin line is PS minimum.

The experimental set-up is shown in Figure 25. A CW wave at 1555.7 nm was modulated with a pseudo-random binary sequence (PRBS) to generate a 10 Gbaud QPSK signal. To emulate the effects of nonlinear phase noise, the signal was coupled through a LiNbO3 phase modulator driven by variable power levels of electrical white noise spanning up to 8 GHz. The signal was amplified to 22 dBm and combined in HNLF 1 (500 m long with nonlinear coefficient 10.7 /W/km, zero dispersion wavelength (ZDW) 1544 nm and dispersion slope (DS) 0.029 ps/nm^2/km) with a 14 dBm portion of pump 1 at 1557.5 nm to generate the FWM comb as shown in Figure 27 (a). The 4f term at 1551.2 nm was de-multiplexed from the comb and injected into a semiconductor laser, providing pump 2. The rest of the comb was passively filtered out leaving the signal and harmonic at 1552.7 nm. These were combined with the pumps in HNLF 2 (300 m long with nonlinear coefficient 10.6 /W/km, ZDW 1553 nm, dispersion slope 0.018 ps/nm^2/km and a strain gradient to increase its stimulated Brillouin scattering (SBS) threshold), with a total pump power of 24 dBm. Any slow relative phase drifts at the PSA input were eliminated by monitoring the signal power at the PSA output and controlling a PZT. The signal was then assessed using a self-homodyne constellation analyser.

The PSA input is shown in Figure 27 (b). The input signal-to-harmonic power offset was 6 dB. The phase sensitive extinction was measured at around 7 dB as shown in Figure 27 (c).

The constellation diagrams in Figure 28 show the regeneration for three added phase noise levels. In the absence of any added noise, there was a slight degradation, see Figure 28 (a) and (b). This stems primarily from the amplification and filtering of the signal within the regenerator, as well as ASE added by the EDFA amplified pumps. Absolute phase deviations of up to 60° per symbol were squeezed down to about 30°; see Figure 28 (c) and (d). The regenerator was able to squeeze even larger phase fluctuations (Figure 28 (e) and (f)), but this was accompanied by phase-to-intensity conversion. It should be possible to suppress this by saturating the PSA. The level of squeezing illustrates one of the key benefits of PSA regenerators – assuming they are placed before a differential receiver, they have the potential to significantly reduce the BER for severely degraded signals. This is because phase deviations are magnified by up to a factor of 2 during differential detection and therefore absolute deviations over ±22.5° for DQPSK can cause errors when differentially decoded, but these can be eliminated by this regenerator. It is worth pointing out that the regeneration of formats containing signalling in both amplitude and phase such as square 16-QAM can be regenerated by placing two such QPSK regenerators in parallel. As such this device truly redefines the possibilities of all optical signal processing.

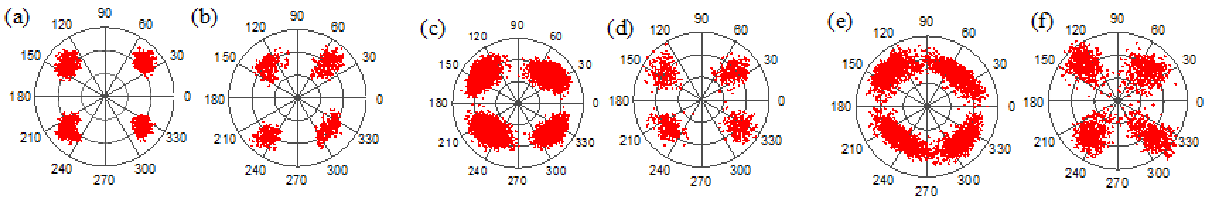

Figure 28: Signal constellations, (a),(c) and (e) regenerator input.

5.5 QPSK Phase and Amplitude Regeneration at 56 Gbaud in a Novel Idler-Free Non-Degenerate Phase Sensitive Amplifier (ORC, UoA)

As discussed in the previous section on “All-Optical QPSK Signal Regeneration in a Novel Multi-Format Phase Sensitive Amplifier”, advanced modulation formats such quadrature phase shift keying (QPSK) are increasingly viable for high capacity optical networks. In line with this, the development of techniques capable of processing multi-level signals represents the logical next step in the nascent field of all-optical information signal processing. Single bit-per-symbol regeneration of phase encoded signals has been demonstrated using degenerate dual pump (2P) PSAs [46]; this approach has been significantly enhanced by a recent scheme allowing black-box operation, with the incorporation of an automatic pump-signal synchronization subsystem [47]. To regenerate QPSK signals, theoretical proposals have included the use of parallel BPSK/DPSK regenerators coherently combined at their outputs [48]. This parallelistic approach, often favoured in electronics, is complicated in optics due to the requirement to equalize and stabilise multiple optical paths (often >100m long with silica fiber implementations) in phase, polarization and propagation delay, which is both complicated and costly. Another proposal utilises a signal-idler conjugate pair transmitted down the link and combined in a non-degenerate (ND) PSA [49]; this however wastes valuable transmission bandwidth, and requires impractically low levels of residual dispersion post–compensation. In Ref. [50] it was recently introduced and demonstrated a new concept, enabling the first demonstration of all-optical QPSK phase regeneration. This utilises a ND four wave mixing (FWM) based parametric amplifier, in which the phase modulated signal interacts with an idler wave bearing a multiple of the temporal phase modulation on the signal. For a QPSK signal, the idler field phase is required to be thrice the signal phase, which was achieved using a first stage incorporating a FWM based coherent phase multiplier, followed by a 2P ND PSA [50]. In this section, a variant of that scheme is presented and experimentally demonstrated, in which phase sensitive gain is obtained directly from a 2P ND parametric amplifier without an idler at the amplifier input, in apparent contradiction to the expected characteristics of a ND PSA. This device configuration, in addition to allowing QPSK phase regeneration in a simpler configuration relying on just one nonlinear element, provides significantly enhanced amplitude noise improvement. We utilize an equivalent time optical sampling oscilloscope to characterize the device's regenerative properties.

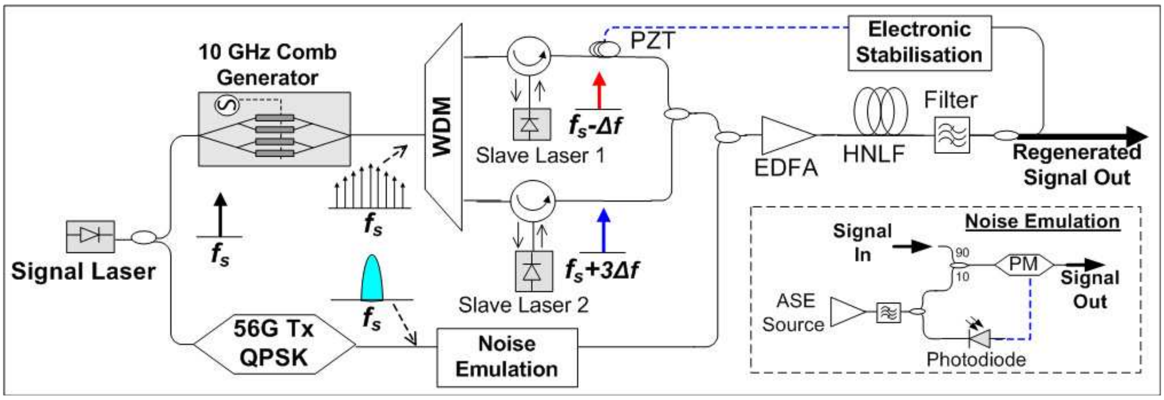

Figure 29: Regenerator setup, Tx – transmitter, WDM – wavelength division demultiplexer, PZT – piezo-electric fiber stretcher, EDFA – erbium doped fiber amplifier, PM – phase modulator, HNLF – highly nonlinear fiber, PM – phase modulator, ASE –amplified spontaneous emission. HNLF parameters are length 300 m, nonlinear coefficient 11.6 /W/km, zero dispersion wavelength 1553 nm and 1550 nm slope 0.018ps/nm2/km.

The experimental set-up is shown in Figure 29. The output of a CW laser at 1555.7 nm was split into two, with one portion coupled into a 10 GHz comb generator. Comb lines at -190 and +570 GHz detuning were injected into semiconductor lasers, providing two pump beams phase locked to the signal carrier. For black-box implementations, the pump-signal synchronization scheme demonstrated in [50] would replace this linear comb. The rest of the signal light was modulated with a pseudo-random binary sequence to generate single polarization QPSK. This was sent through a noise additive module to emulate the effects of linear (related to quantum noise and ASE) and nonlinear phase noise (related to nonlinear amplitude to phase conversion). This module (shown as an inset in Figure 29) comprised an ASE source whose output was split into two, one portion being detected and the resulting electrical white noise being used to drive a LiNbO3 phase modulator through which the signal was passed, and the other portion being optically combined with the signal in a coupler. The signal was then combined with the pumps and all the waves were amplified in an EDFA, leading to 50 mW of signal power and 250 mW power per pump. They were then sent into an HNLF, which has a strain gradient to increase its stimulated Brillouin scattering threshold, allowing the use of continuous wave pumps. Slow thermo-acoustic relative phase drifts were suppressed by monitoring the signal power at the PSA output and controlling the PZT. The signal was then assessed using an EXFO constellation analyzer (PSO-200) based on all-optical sampling capable of operation up to 100 Gbaud.

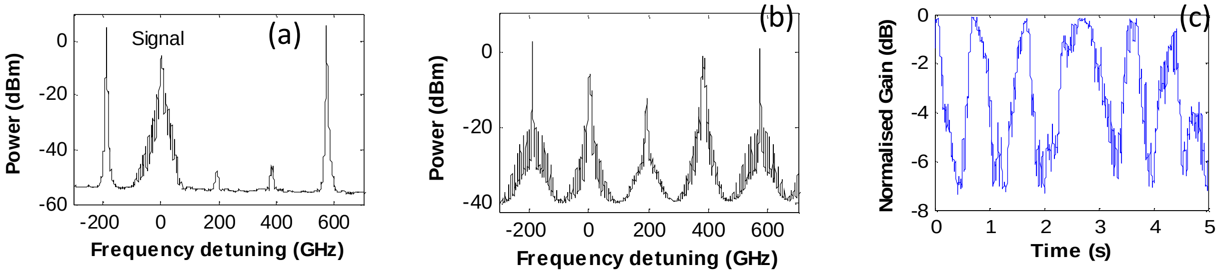

Figure 30: (a) Illustration of how amplification of I and Q quadratures is achieved while 45° component is de-amplified. White circles, input , dotted vector , black circles, output (b) Example with symbols at 30° and 80° (c) Complete semi-analytical transfer function showing phase and amplitude response. (d) Regeneration in two steps – 1) Nonlinear generation of phase harmonics via FWM followed by pump recovery, 2) Parametric phase sensitive gain.

The input and output spectra to the PSA are shown in Figure 30 (a) and (b). At the input to the PSA, there is negligible power at the idler frequency (+380 GHz detuning); a very weak component emanating from weak FWM in the high power EDFA is visible but at -40 dB relative to the signal this does not affect the subsequent parametric interaction as verified by numerical simulations. 7 dB phase sensitive gain variation was obtained at the PSA output as measured with the feedback to PZT turned off (Figure 30 (c)). The spectrum at the output to the PSA (Figure 30 (b)) suggests two separate interactions occur simultaneously – first, the presence of the strong component at +190 GHz detuning indicates coherent phase multiplication via mixing of the signal with the pump at -190 GHz, and the strong idler at +380 GHz indicates conventional 2P phase insensitive amplification. We believe the coherent interplay between these two interactions leads to the phase sensitive gain, with the transfer characteristics originating from the same principles as in [50]. This will be analytically and numerically studied further in due course. The regenerator was first characterized at 10 Gbaud with phase noise only. Pseudo-Gaussian phase fluctuations would be expected at the input, with an artificial roll-off at the tails of the distribution due to the saturation of the photodiode for high ASE levels. The color grade signal constellations including data on the phase error variance and normalised variance of amplitude noise are shown in Figure 31. While this statistical information would be more robust if obtained from a homodyne receiver without digital phase compensation for the intradyne local oscillator, it is still useful for quantifying relative signal improvements derived from the regenerator. The regenerator reduced the phase error variance by a factor of 6, while the amplitude noise variance only increased by 2.6, hence an overall benefit (Figure 31, Cell A). This phase noise reduction is comparable to the numerically predicted factor of 5.5 for the parallel BPSK regenerator scheme [48], denoting that the inline compactness of our approach does not come with an associated performance penalty. For QPSK, a comparison with studies on the impact of phase estimation errors on BER suggests that the output phase error variance of 0.0042 rad^2 (Figure 31, Cell A) approximately corresponds to an SNR penalty under 0.5 dB for a BER of 10-4, while the input variance corresponds to a penalty >>4 dB [[51]]. This nonlinear phase noise reduction implies that i) the reach of the transmission span can be increased ii) the tolerance to nonlinearity is significantly enhanced; hence higher receiver OSNRs can be envisaged. In the presence of linear phase noise, the phase error variance and normalised amplitude variance are simultaneously reduced by approximately 3.2, indicating even better net regenerator performance (Figure 31, Cell B). This ability to concurrently reduce both absolute phase and amplitude variance prior to the receiver suggests that the regenerator should provide a BER improvement if deployed before a differential receiver, which normally requires a trade-off between reduced complexity and lower noise tolerance compared to a fully coherent one. The symbol rate was increased to 56 Gbaud. Without added noise, the regenerator preserves the phase quality at the expense of some amplitude noise (Figure 31, Cell C). We believe this is a result of multiple parametric interactions occurring in the PSA that transfer some amplitude noise to the signal. In the presence of phase noise, the phase error variance is reduced by a factor of 3.2, with increased amplitude noise at the output (Figure 31, Cell D). For QPSK however, in which the information is solely contained in the phase, this increased nonlinear phase noise tolerance would translate to increased reach or higher signal launch powers to improve OSNR at the receiver.

10 Gbaud (20 Gbit/s)		56 Gbaud (112 Gbit/s)	
INPUT	**OUTPUT**	**INPUT**	**OUTPUT**
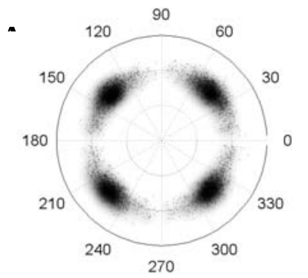 $\sigma^2_{\Delta\theta} = 0.0258$ $\sigma^2_{\Delta rho} = 0.0062$	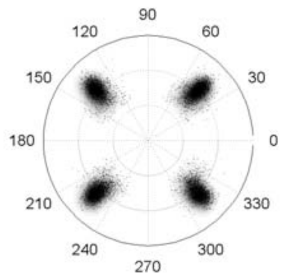 $\sigma^2_{\Delta\theta} = 0.0042$ $\sigma^2_{\Delta rho} = 0.0163$	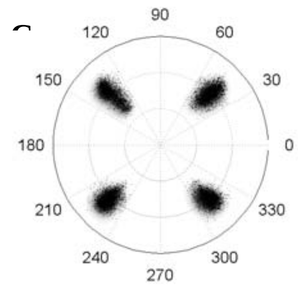 $\sigma^2_{\Delta\theta} = 0.0023$ $\sigma^2_{\Delta rho} = 0.0148$	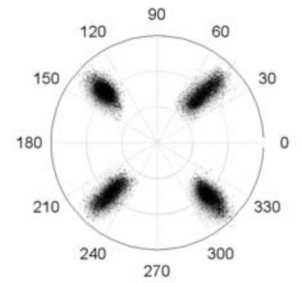 $\sigma^2_{\Delta\theta} = 0.0023$ $\sigma^2_{\Delta rho} = 0.0257$
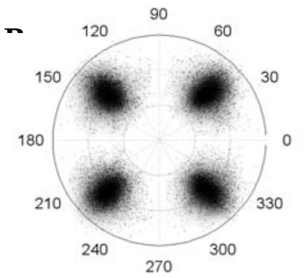 $\sigma^2_{\Delta\theta} = 0.0165$ $\sigma^2_{\Delta rho} = 0.0347$	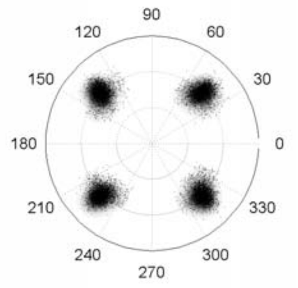 $\sigma^2_{\Delta\theta} = 0.0048$ $\sigma^2_{\Delta rho} = 0.0108$	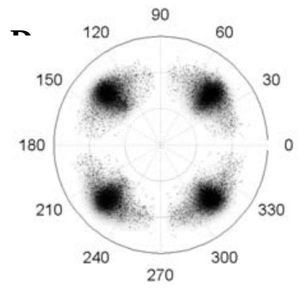 $\sigma^2_{\Delta\theta} = 0.0206$ $\sigma^2_{\Delta rho} = 0.0143$	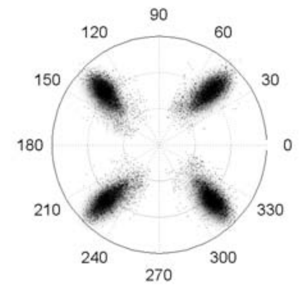 $\sigma^2_{\Delta\theta} = 0.0064$ $\sigma^2_{\Delta rho} = 0.0368$

Figure 31: Regenerator input and output constellation data at 10 and 56 Gbaud – $\sigma^2_{\Delta\theta}$ is the phase error variance, $\sigma^2_{\Delta rho}$ is the normalised amplitude noise variance.

5.6 Numerical simulation of photonic systems: Application to optical regeneration (USWAN)

5.6.1 Software tool development: pulseprop

A piece of software (pulseprop) is developed to be both efficient and adaptable and is applied to the subject of optical regeneration in order to test its suitability. This in-house software tool makes use of the 4th-order (global) Runge-Kutta in the interaction picture method [52] to propagate the field through each fibre. It uses adaptive step-size to reduce computation time and a small error tolerance to guarantee high accuracy. A particular version of an optical regenerator is studied [53] which involves spectral broadening due to non-linear interactions of high peak power pulses within optical fibre. An important consideration for the optical regenerator is its optimisation as well as typical metrics for the improvement of the output signal compared to the input. There is the possibility of combining the regenerator with other functions, such as wavelength conversion and buffering, to produce an all-optical router.

5.6.2 Regenerator performance evaluation

This work explores the effects of passing a noise impaired bit-stream through a two-stage regenerator multiple times [54]. A second stage is usually used to recover the original signal wavelength, which is shifted at the exit of the first stage. By optimising the parameters for each stage of the regenerator it is possible to suppress amplitude jitter, while also reducing timing jitter incurred by the first stage. Multiple passes through the two stage regenerator are studied in order to assess whether further amplitude jitter suppression (or reduction) is possible, and whether timing jitter places a restraint on the total number of such passes. The proposed scheme is introduced followed by the simulation parameters. Qualitative and quantitative information is given along with eye diagram and Q-factor in order to evaluate the effectiveness of multiple passes through this system.

A5.6.2.1 Principle of operation

Figure 32 shows a double-cell SBF regenerator where a second cell is placed after the offset filter of the first cell. Within this second cell, the offset frequency is changed so that the original centre frequency of the pulses is recovered. The second EDFA boosts the pulse peak power to a lower value that of the first cell amplifier.

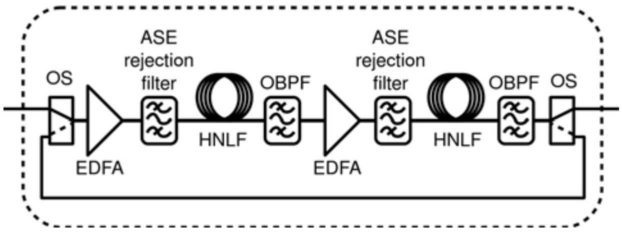

Figure 32 Schematic of the simulations set-up. EDFA: Erbium-doped fibre amplifier; OS: optical switch; HNLF: highly nonlinear fibre; OBPF: optical band-pass filter.

A5.6.2.2 Simulations parameters

Regenerator parameters were optimised, taking into consideration guidelines [55, 56, 57, 58], and are shown in Table 3. A pseudo-random bit stream (PRBS) was generated consisting of 256 bits with 256 samples per bit. Each one bit has a Gaussian pulse positioned at its centre, with pulse width 6.25 ps full-width at half of maximum (FWHM) at a carrier wavelength of 1550 nm. Noise was added to this bit stream by adding a pseudo-random amplitude variation to each sample, followed by filtering with a 5^{th}-order Super-Gaussian filter with bandwidth 150 GHz (FWHM).

When entering the first SBF-cell the pulses have their peak power set to 3.3 W by suitable setting of the EDFA output average power. After passing through the HNLF the pulses are filtered at a frequency offset of 375 GHz, by a Gaussian filter of width ≈ 70 GHz (FWHM). After leaving the first SBF-cell, the pulses are amplified in the second cell to a peak power of 3.1 W before entering a HNLF with same parameters as in the first cell. The pulses are again filtered, this time at their original frequency (using an offset of -375 GHz relative to the current frequency). On output of the second cell the pulses are either directed out of the regenerator or fed back to the first cell through the use of an optical switch. Within the simulation the feedback was achieved by explicitly setting a total number of loops.

Parameter	Symbol	Value	Unit
Attenuation coefficient	α	2.13	dB/km
Length	L	1.0	km
Nonlinear parameter	γ	18	$(W \cdot km)^{-1}$
Dispersion parameter	D	-1.7	ps / (nm·km)
Dispersion slope	S	0.023	ps / (nm^2·km)

Table 3 Regenerator parameters and values used for the loop simulations.

A5.6.2.3 Simulations results and discussion

Figure 33 (left) illustrates the eye diagram at the output of the first cell amplifier. The Q-factor is 9.94dB at optimised threshold level. At the exit of the dual-cell the amplitude jitter and noise level are clearly reduced as shown in Figure 33 (middle). The Q-factor improvement for one loop is 4.70dB. Investigations for higher number of loops have shown that the Q-factor improvement becomes negligible after 5 loops. Therefore the maximum Q-factor improvement obtainable for the studied case is 9.36dB, which means a double increase of final Q-factor.

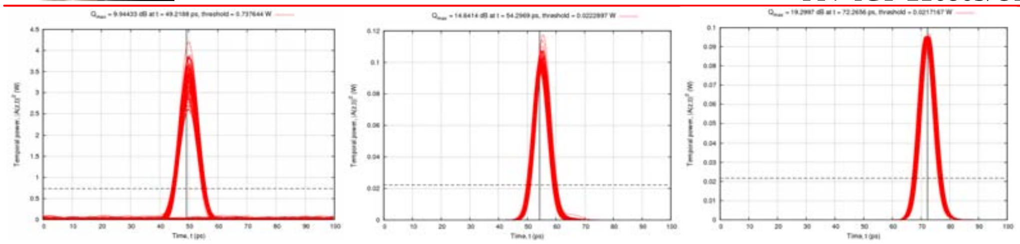

Figure 33 Eye diagram at the output of the first cell amplifier (left) and output after the second cell filter (middle) during the first loop and at the output of the two-cell regenerator after 5 loops (right).

5.6.3 Conclusion

The results show that a two-cell SBF regenerator is advantageous over a single-cell version. It allows recovery of signal wavelength, increased amplitude jitter suppression, and reduces timing jitter. Additional loops through the device continue to show favourable reduction in amplitude jitter through the Q-factor difference (between successive loops). Simulations have shown that Q-factor improvement becomes negligible after five loops. In the studied case, the Q-factor has doubled after five loops demonstrating the efficiency of the proposed optical regenerator scheme. In addition the output signal has negligible noise at the zero level and significant amplitude jitter suppression.

6. Monitoring (Telecom Bretagne, UC3M, UMons, DTU, HWDU)

6.1 Evolution of an OPM prototype for In-Band OSNR measurements (Telecom Bretagne)

6.1.1 Automatic acquisition of in-band OSNR values with the OPM prototype

In work that had started in Year 2 of the project, a free-space OPM prototype is modified with the integration of a Polarization Controller (PC) at the input of the prototype and a Linear Polarizer (LP) in between the first lens and the diffraction grating (Figure 34) to perform in-band OSNR measurements. Data collected on the array is treated with LabVIEW^{TM} via an acquisition card. A combined time of 17 ms (sensor read time and data treatment time) is required to acquire one value from the camera. This value is a limiting factor impacting on the duration of the OSNR measurement. During the scanning of the PC, power values relative to the channels are recorded N times, with their respective extremum values finally leading to the evaluation of their OSNR. The OSA serves to establish reference OSNR values with respect to a resolution of 0.1 nm. We recall the systematic difference of around 3.3 dB between in-band OSNR values measured with the OSA and the OPM, which is due to the distinction in size and form of the transfer function of the instruments.

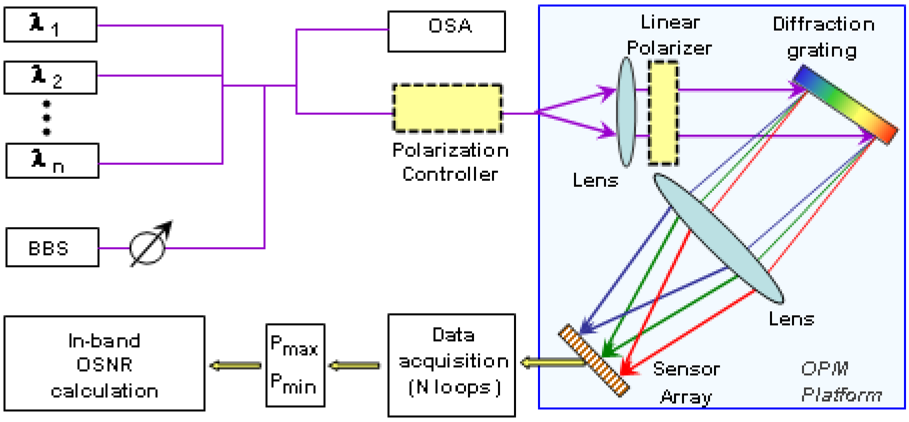

Figure 34. Experimental set up for automatic acquisition of in-band OSNR values.

6.1.2 Relationship between acquisition time and measurement dynamics

The accuracy of the in-band OSNR measurement is conditioned mainly by the extinction ratios of the LP (1/η) and the PC (1/C):

$$\frac{1}{OSNR_{meas}} = \frac{1}{OSNR_{real}} + 2\left(\frac{1}{\eta} + \frac{1}{C}\right) \tag{1}$$

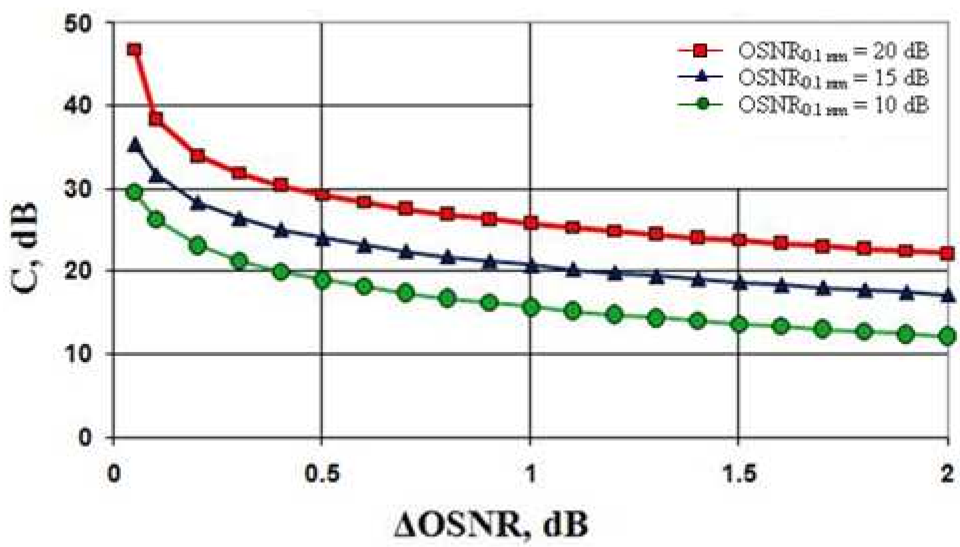

Figure 35 Relationship between the dynamics of the PC and the precision on the in-band OSNR measurement ($\eta = 10^4$).

It can be clearly seen on the above graph that for a fixed η of 10^4, the contrast required on the PC to achieve a particular precision on the OSNR value increases with the latter.

For a single-channel OSNR measurement, it would be highly recommended to use an algorithm [59] to accelerate the convergence of the signal SOP towards the desired one to improve the measurement time. However, for a multi-channel configuration, this would prove quite complex to achieve with each channel likely to have a different input SOP. It seems, henceforth, more convenient to use the PC in an open loop configuration so as to function as closely as possible as a perfect time-averaging polarization scrambler. In this respect, we can define a lower bound for the measurement time for a given OSNR. We show that for a given input signal SOP, the proportion of the SOP at the output of the PC (via a perfect LP) bearing a contrast of at most 1/C with the former is 1/C (for C>>1). Considering a uniform scanning of the Poincare sphere by the PC, the measurement time for a given OSNR with a particular precision value will be $T_{meas} \geq CT_{acq}$, where T_{acq} is the time taken to acquire one value on the sensor array.

6.1.3 Experimental results

The PC consists of 4 quarter wave plates rotating at several scanning rates. We first evaluate the precision of the OSNR measurement, Δ_{OSNR} for 5 scan rates of the PC (SR_8 being the fastest). A single channel is used for a reference $OSNR_{0.1\ nm}$ value of 18 dB. Figure 36 (secondary axes) represents 10 Δ_{OSNR} values, each obtained for N=1000 acquisitions (~17s) by the sensor array for various SR. SR_6 seems to yield the best results. This is probably due to the fact that the SOP fluctuation is too rapid for the sensor at faster SR.

SR_6 is then used to evaluate the impact of N for 10 Δ_{OSNR} values at an $OSNR_{0.1\ nm}$ of 18 dB (Figure 36, main axes). The precision is better than 0.6 dB as from N = 1200.

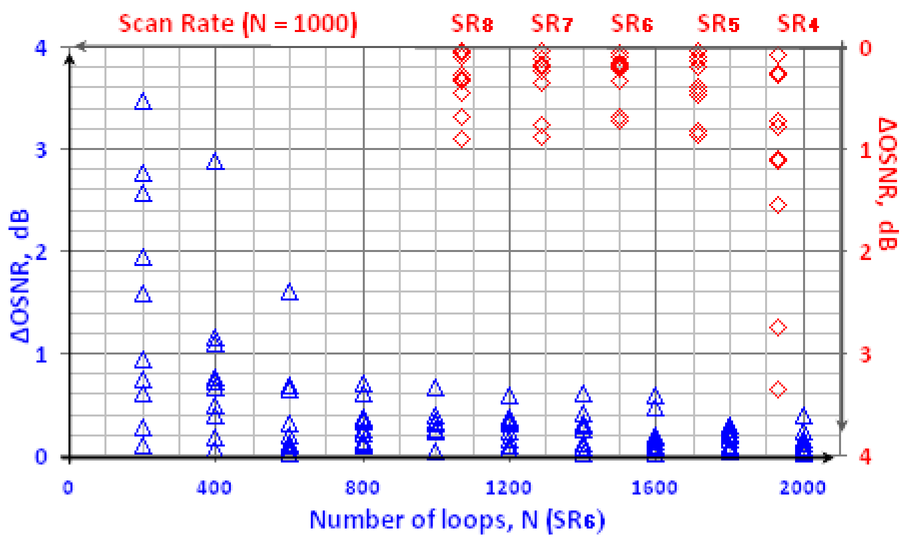

Figure 36 Δ_{OSNR} as a function of the number of values acquired (main axes) and the scanning rate of the PC (secondary axes).

We finally measure automatically OSNR values for a group of 8 C-band channels for 3 reference $OSNR_{0.1\ nm}$ values of 10, 15 and 18 dB (Figure 37). For each channel, 10 Δ_{OSNR} values are recorded at SR_6 for N = 2000. For an $OSNR_{0.1\ nm}$ of 18 dB, the worst Δ_{OSNR} values are close to 0.5 dB. As expected, the scattering of the Δ_{OSNR} values is more pronounced for larger OSNR.

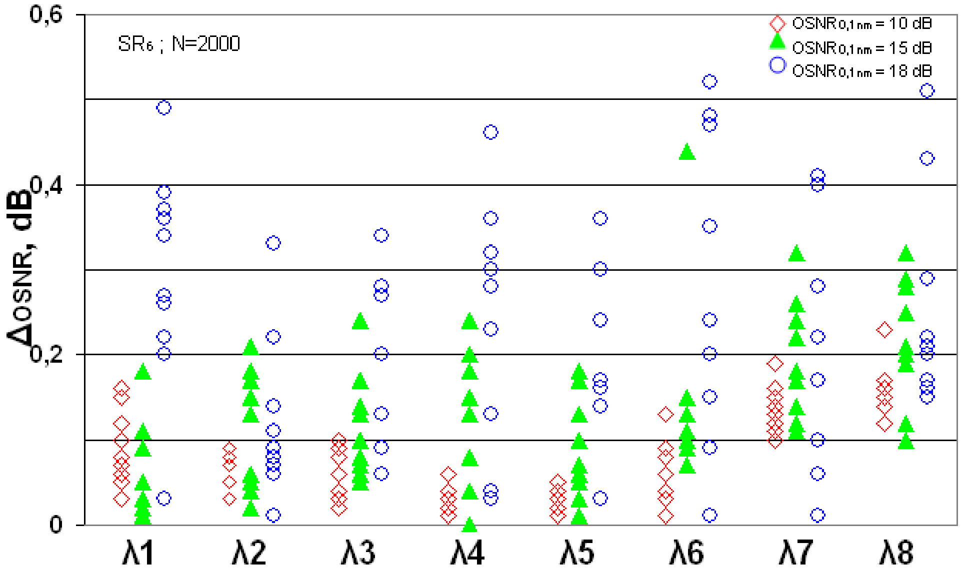

Figure 37 Δ_{OSNR} for an 8-channel system for 3 $OSNR_{0.1\ nm}$ values.

6.1.4 Conclusion & perspectives

We have modified an OPM prototype to carry out automatically parallel in-band OSNR measurements on a multi-channel system. This parallel method is slower than a single-channel technique since it is impeded by the data acquisition time on the sensor array and the PC must be used in an open loop configuration. However, it becomes competitive as from the monitoring of a dozen of channels. There exist commercial detector arrays that are 5 times as fast as the one at our disposal. Faster acquisition sensor array time offers the possibility to use faster scanning rates of the PC, which in turn allows us to believe that there it should be possible to drastically reduce the measurement time of in-band OSNR.

6.2 Reflective self-referencing attenuation measurements in metro WDM networks (UC3M)

A low-cost monitoring system for measuring the optical power losses of drop fibres in Wavelength Division Multiplexing (WDM) Passive Optical Networks (PON) is developed. The proposed system is based on Radio-Frequency (RF) intensity modulation and Fibre Bragg Grating (FBG) self-referencing measurement techniques using amplitude normalization. The monitoring unit is built with an optical Broadband Light Source (BLS) illuminating the PON from the Central Office (CO) for testing purposes, and the signal processing of the measurements is provided by low-frequency analog filters and a lock-in amplifier. The system allows measuring the optical power losses of the PON branches independently, with increased sensitivity in a re-configurable and flexible way. The monitoring technique has been studied and experimentally validated in a Coarse WDM-PON prototype, as a first approach to Dense WDM-PON applications. This work has been published in Ref. [60] and has also been included in the WP15 poster which was presented at ECOC 2010.

6.3 Long-haul Joint Channel Parameters Estimation in Ultra-Long-Haul WDM Transmission Experiments with Coherent Receivers (PoliTo)

We investigated the use of advanced channel monitoring techniques, required by increasingly sophisticated high-capacity and long-distance optical networks [61], in a challenging experimental scenario where a Terabit superchannel, composed of 10x(30 Gbaud) PM-QPSK subcarriers, is transmitted over 8000 km of PSCF.

6.3.1 Experimental set-up

The experimental setup is shown in Figure 38. Fifteen CW wavelengths spaced 66 GHz were modulated using a NMZ modulator, provided by OCLARO, to generate a 15-subcarrier signal, with each subcarrier carrying 60 Gb/s. This WDM signal was then narrow-filtered using a reconfigurable Finisar optical Waveshaper™ filter, with -3dB bandwidth 33 GHz. This filter is capable of generating all passbands at once, so only one filter unit was used. In addition to narrow filtering, the Waveshaper filter profile was set to enhance the high frequency components of each QPSK subcarrier to pre-compensate for electrical bandwidth limitations both at the Tx and Rx. All fifteen 66-GHz spaced QPSK subcarriers were then launched into an optical frequency-doubler, comprising a pass-through branch and a frequency-shifter (FS) branch. The latter included a NMZ modulator operated as a FS, configured to shift the fifteen input subcarriers by 33 GHz. The pass-through and FS branches were delayed for decorrelation and then combined to form a 30-subcarrier, 33-GHz spaced QPSK-modulated signal. This signal was then polarization multiplexed to form a 30-subcarrier PM-QPSK signal, with 33GHz spacing. Each PM-QPSK subcarrier carries 120 Gb/s.

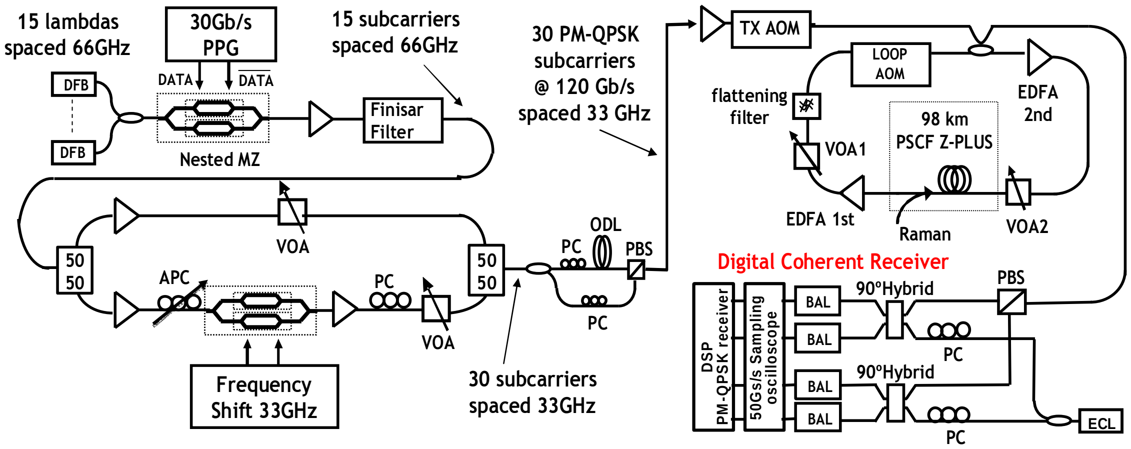

Figure 38. Experimental set-up for the 3x1.2 Tb/s superchannels. DFB: distributed-feedback laser, MZ: Mach-Zehnder, PPG: pulse pattern generator, ODL: optical delay line, PBS: polarization beam splitter, AOM: acusto-optic switch, EDFA: erbium doped fiber amplifiers, VOA: variable optical attenuator, BAL: balanced photodetector, PC: polarization controller, APC: automatic polarization controler, ECL: external cavity laser.

The signal was then launched into a recirculating fiber loop consisting of 98.1-km of uncompensated Z-PLUS® PSCF. The fiber loss is 17.6 dB. Nominal dispersion at 1550 nm is 20.6 ps/nm/km, slope 0.06 ps/nm^2/km. The effective area is about 110 μm^2. Backward Raman amplification was used with a net gain of 9.2 dB. A three-pump Raman source with a total power of 800 mW was employed, at 1425, 1436 and 1459 nm. The loop included a dual-stage

EDFA as well. A gain-flattening filter, the loop acousto-optic switch and the 3 dB coupler were inserted between the EDFA first and second stage.

The Rx had a standard set-up for coherent reception, with a LO and two 90-degree hybrids. The eight outputs of the two hybrids were detected using linear-amplified dual-balanced photodetectors with 30 GHz bandwidth provided by Linkra-Teleoptix. Subcarrier selection was performed exclusively by tuning the LO. The four photodetectors electrical signals were digitized at 50GSa/s using a Tektronix DPO71604 real-time scope. The sampling rate was 1.66 samples/symbol. The measured scope analog -3dB bandwidth was only 12 GHz, i.e., 0.4 times the Baud rate. It was compensated for by Tx optical pre-emphasis, as mentioned, and by the Rx DSP equalizer.

The Rx DSP consisted of a CD-compensation first stage followed by a 25-taps MIMO stage adjusted through a decision-driven CMA algorithm, followed in turn by frequency estimation and a Viterbi&Viterbi stage. Tx and LO lasers were two distinct, external-cavity lasers (ECL), with linewidth of about 100 kHz. At the Tx, the ECL was tuned to each channel position, replacing each DFB source in turn, for BER measurements.

6.3.2 Channel estimation results

For each of the thirty subcarriers, performance monitoring algorithms similar to those described in [62, 23] have been applied, after 8,000 km transmission (82 recirculations), to estimate CD, PMD, PDL and the electro-optical transfer function $|H(f)|^2$.

An example of the plots obtained for subcarriers 18 and 28 is shown in Figure 39. The plots relative to the estimation of PDL, DGD and CD are shown only in the range [-15, 15] GHz, since the values that fall outside the cut-off bandwidth of the Rx are not significant. The lower left plot shows the estimated electro-optical transfer function of the system. This plot can be used as an indicator of the correct tuning of the Tx laser and the optical shaping filter: if the passband of the filter is not centered at the laser emitting frequency, the plot of $|H(f)|^2$ is asymmetric (see Figure 39, dashed line).

Figure 40 shows the results of long-term measurements (several hours) in terms of DGD and PDL at $f = 0$ on the center channel (6th) of the single superchannel transmission with subcarrier spacing equal to the Baud rate. The values of measured BER are also shown for reference. We have verified through simulations that the monitor is able to estimate the correct PDL value regardless of the relative angle between the signal state of polarization (SOP) and the PDL axis, while the monitored DGD value depends on the direction of the signal SOP with respect to DGD vector (the estimated value may vary from 0 to the actual DGD). The variations of DGD in Figure 40 (left) are mainly due to this effect and consequently are not related to the value of BER, since DGD can be completely compensated for by the equalizer.

On the contrary, the estimated values of PDL in Figure 40 (right) correspond to the actual PDL present in the system at time of measurement and are strictly related to the values of BER: while the effects on PDL on the signal power variations can be compensated for by the equalizer, the performance is nevertheless degraded by the effects of PDL on noise. Note that such high values of PDL (up to 5-6 dB) are due to the specific transmission setup, made of a large number of recirculations of identical single-span links.

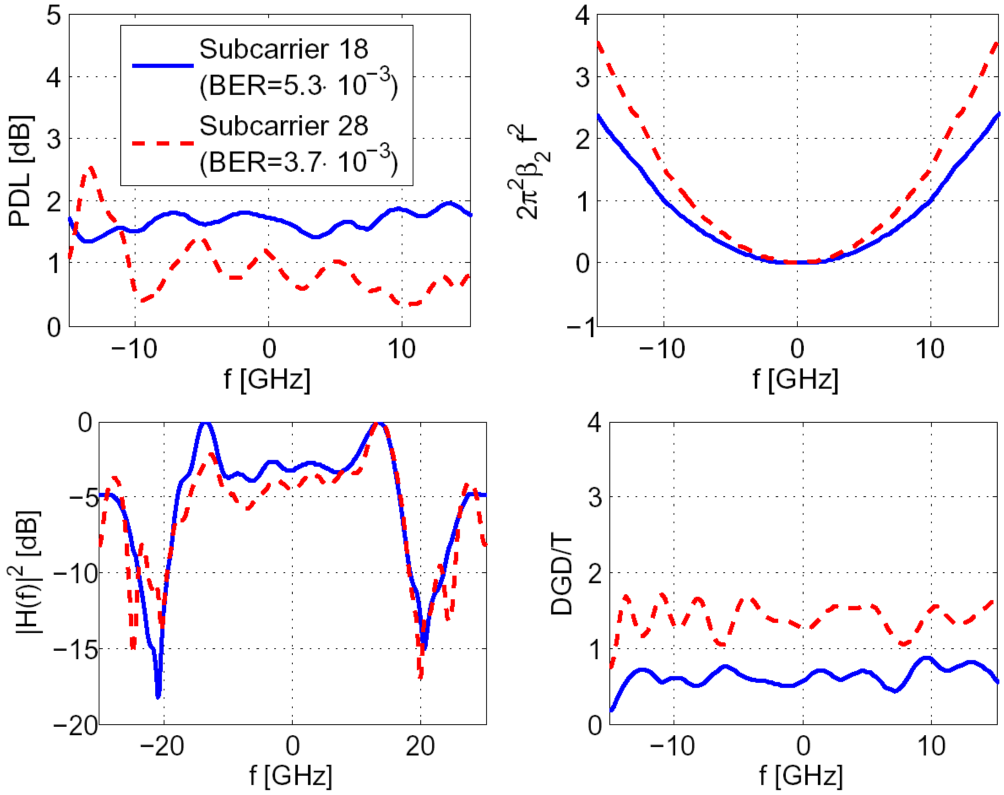

Figure 39. Example of channel estimation outputs for subcarrier 18 and 28.

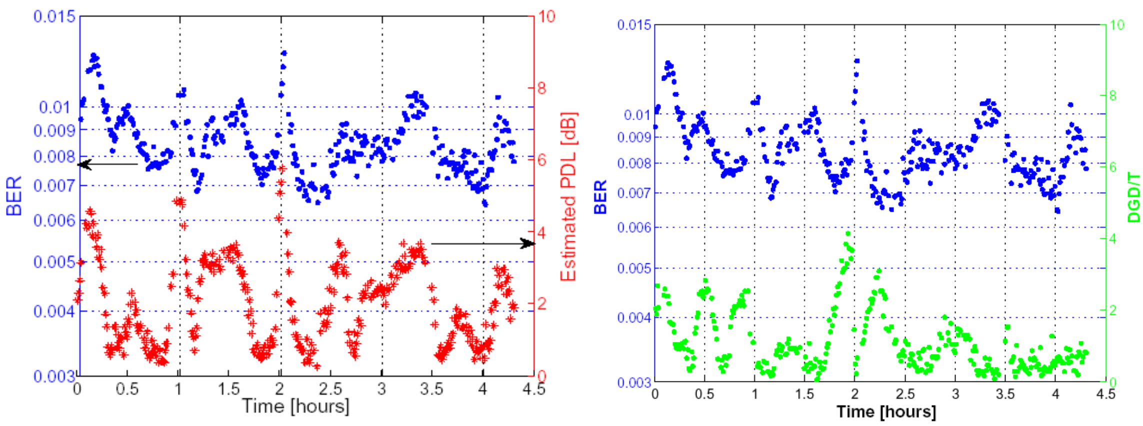

Figure 40. Long term measurement on center channel. Left: . BER and estimated PDL. Right: BER and estimated DGD.

6.4 Data-Aided Channel Estimation Based on Constant-Amplitude-Zero-Autocorrelation (CAZAC) Sequences (DTU and HWDU)

6.4.1 Introduction

Constant Amplitude Zero Autocorrelation (CAZAC) sequences have been demonstrated as a promising training sequence candidate for data-aided optical channel estimation in 112 Gbit/s polarization-diversity coherent systems. Extensive numerical investigations show accurate chromatic dispersion estimation for different OSNR conditions including the case for 10 dB. In addition to different noisy scenarios, the robustness of the estimation has been demonstrated over a wide range of combined distortions including random PMD contributions ranging from 10 to 35 ps and 6 dB of PDL. Despite of non-data-aided approaches, estimation processes using CAZAC sequences and the zero-forcing criteria are independent of memory lengths and update algorithms for FIR filter taps convergence. Additionally, an estimation approach of instantaneous differential group delay parameter has been demonstrated for high values of OSNR. Therefore, data-aided channel estimation based on the principle of zero-forcing and using CAZAC sequences as training sequences, opens the door to accurate and low complexity approaches toward real time implementation of optical performance monitoring algorithms.

6.4.2 Description

The CAZAC is a complex-valued phase-noise (PN) sequence with a constant amplitude and periodic zero-autocorrelation. The discrete CAZAC is defined as follows:

$$c[n] = \begin{cases} \exp(jK_c \pi n^2 / L_c), & L_c : even \\ \exp(jK_c \pi (n-1)^2 / L_c), & L_c : odd \end{cases} \qquad (1)$$

where L_c denotes the number of samples per CAZAC and K_c is a constant integer. The discrete CAZAC sequence has constant amplitude and the sample values are on the unit circle. The CAZAC sequence is additionally zero-mean.

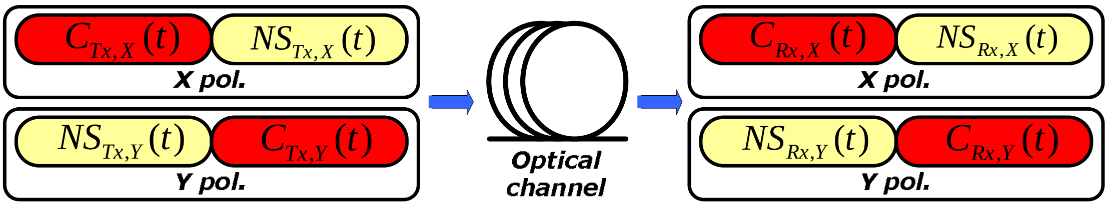

Figure 41: Schematic diagram of the transmitted and received training sequences for both polarizations to estimate the MIMO optical channel.

In order to estimate the optical channel, a training sequence of length *2n* is divided into two sub-sequences and sent it respectively over the two polarizations *X* and *Y*. One of the transmitted sub-sequences is a CAZAC sequence of length *n* ($C_{Tx,X}(t)$ for polarization *X*) which is allocated in orthogonal time-slots from polarization to polarization (see the red-block in Figure 41). The other transmitted sub-sequence is a "non-signal (NS)" sequence of length *n* ($NS_{Tx,X}(t)$ for polarization *X*). The four MIMO components of the inverse channel transfer function $\overline{W}_{ZF}(f)$ can be estimated applying the zero-forcing criteria to calculate the relations shown in Eq. 2.

$$\overline{W}_{ZF}(f) = \begin{pmatrix} W_{xx}(f) & W_{yx}(f) \\ W_{xy}(f) & W_{yy}(f) \end{pmatrix} = \begin{pmatrix} \dfrac{C_{Rx,X}(f)}{C_{Tx,X}(f)} & \dfrac{NS_{Rx,X}(f)}{C_{Tx,Y}(f)} \\ \dfrac{NS_{Rx,Y}(f)}{C_{Tx,X}(f)} & \dfrac{C_{Rx,Y}(f)}{C_{Tx,Y}(f)} \end{pmatrix} \qquad (2)$$

A6.4.2.1 Chromatic dispersion estimation and polarization effects estimation (DGD and PMD)

To estimate ψ and the residual CD, it is firstly defined the function $Z(f)=\sqrt{\det(\bar{W}_{ZF}(f))}$. The phase transfer function $\hat{H}_{CD}^{-1}$ can be estimated with a quadratic fit after unwrapping the π-ambiguity from the phase transfer function of $Z(f)$.

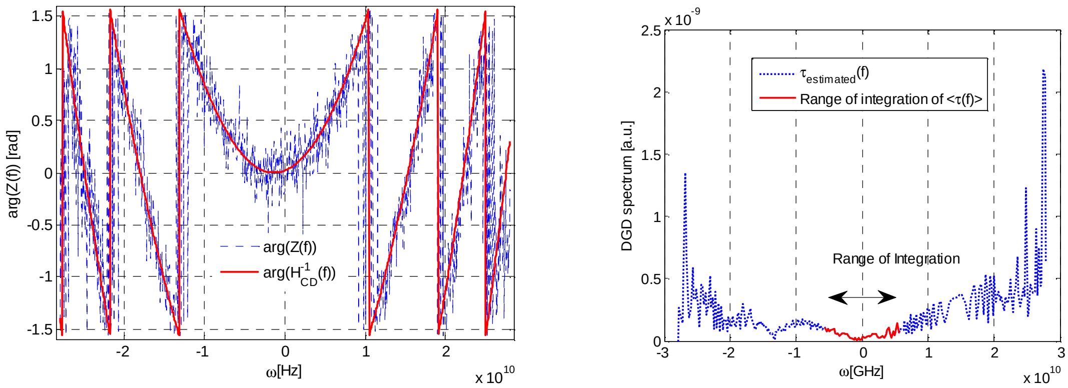

Figure 42: (a) Phase transfer function of $Z(f)$ after MIMO channel estimation based on the CAZAC sequence and the estimated CD dispersion function by the quadratic function. 2(b) Illustration of the range of integration over a DGD spectrum for estimation of $\langle\tau(f)\rangle$.

Figure 42 (a) shows the noisy parabolic function calculated from the phase transfer function of $Z(f)$ and the estimated phase transfer function $\hat{H}_{CD}^{-1}$ after the quadratic fit. A reliable DGD estimation can be achieved by averaging the DGD spectrum over a certain bandwidth as it is shown in Figure 42 (b). Eq. 4 and 5 describe mathematical operations required to cancel CD and PDL contributions for DGD estimation.

$$\bar{W}_{UE}(f)=\frac{\bar{W}_{ZF}(f)}{Z(f)}=\prod_{i=N,-1}^{1}\begin{pmatrix}u_i^*(f) & -v_i(f)\\ v_i^*(f) & u_i(f)\end{pmatrix}\begin{pmatrix}k_i^{1/2} & 0\\ 0 & k_i^{-1/2}\end{pmatrix}=\begin{pmatrix}u_I(f) & v_I(f)\\ v_{II}(f) & u_{II}(f)\end{pmatrix} \quad (3)$$

$$\tau_{estimated}(f)=2\sqrt{u_{I,\omega}(f)u_{II,\omega}(f)-v_{II,\omega}(f)v_{II,\omega}(f)} \quad (4)$$

Figure 42 (b) shows a DGD spectrum for an inverse channel transfer function.

6.4.3 Main results

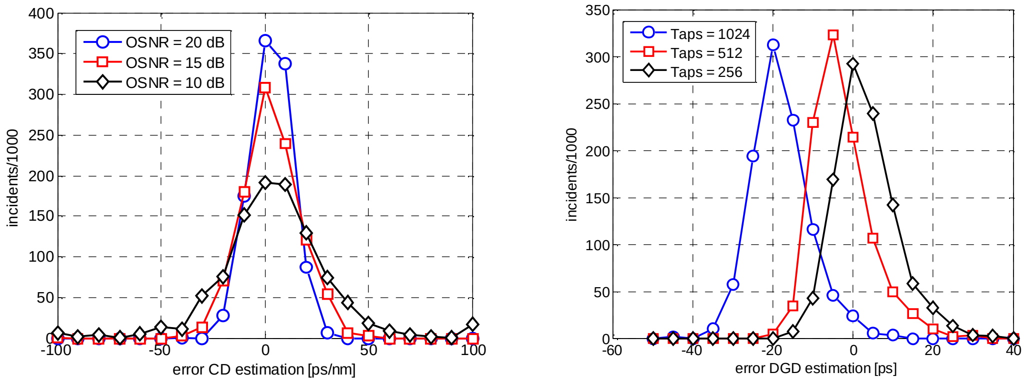

Figure 43: (a) Error CD estimation curves for OSNR values of 10 dB, 15 dB and 20 dB respectively. The length of the CAZAC sequence generated was fixed to 128 taps. 3(b) Error DGD estimation curves for three different simulated scenarios with CAZAC sequences of length 128, 256 and 512 taps respectively. The OSNR value in all cases was fixed to 50 dB and the CD to 1000 ps.

OSNR [dB]	Number of taps	m_{CD}	σ_{CD}
10	256	7.5172	50.1325
	512	4.0048	34.3923
	1024	2.5240	12.5384
10	256	7.5172	50.1325
15		2.7493	20.3875
20		2.9101	9.4226

Table 4: Summary of mean and deviation values of the CD estimation process for six different simulated scenarios. The first three rows report the estimation statistics when an OSNR value is fixed and the length of the CAZAC sequence vary. The last three rows report the estimation statistics when the length of the CAZAC sequence is fixed while the OSNR values vary.

Resolution (taps)	Range of averaging (taps)	m_{DGD}	σ_{DGD}
256	16	4.0558	7.5744
	12	2.3545	7.1209
	16	0.7863	6.8502
1024	14	-17.9779	7.0947
512		-2.6859	7.1412
256		3.2632	7.5401

Table 5: Summary of mean and deviation values of the DGD estimation process for six different simulated scenarios. The first three rows report the estimation statistics when the length of the CAZAC sequence is fixed and the range of integration around the central tap on the DGD spectrum vary. The last three rows report the estimation statistics when the length of the range of integration is fixed and the length of the CAZAC sequence vary.

6.5 Novel approaches for monitoring drop fibres in TDM-PON and WDM-PON systems (UC3M/UMons)

Passive Optical Networks (PON) are progressively becoming reality while commercial deployments are reported worldwide. Operating these networks requires adequate means for a cost-effective monitoring and is of great importance for operators. FPMs and UC3M recently proposed two different physical layer monitoring techniques for PONs. The purpose of the STM was combining these techniques and applying to PONs or WDM-PONs in order to be able to monitor the network and measure the temperature simultaneously. This work is presented in Ref.[63].

7. Other Research Activities (CTTC, UMons, UPVLC)

7.1 OFDM-based optical direct-detection systems (CTTC)

Optical orthogonal frequency division multiplexing (O-OFDM) represents an attractive technology for next generation optical networks thanks to its scalability to high-speed transmission and its robustness against channel dispersions. It has rapidly gained attention in the optical community, also due to the progress in electronic digital signal processing (DSP) for optical communications.

High performance systems in terms of spectral efficiency, receiver sensitivity and robustness against dispersions are reported for long-haul transmission using coherent detection. Nevertheless, O-OFDM results also attractive for cost-sensitive applications based on direct detection (DD). In fact, DD systems are simpler than coherent schemes and can be implemented by using commercial components [64].

A cost-effective implementation of the O-OFDM technique is the discrete multitone (DMT) modulation, that can find application in high-speed optical LANs, 10Gb/s Ethernet using multimode fiber, interconnects in data centers and high performance computing [64, 65, 66, 67]. We have proposed a novel power-efficient O-OFDM transmission system based on the discrete Hartley transform (DHT), for cost-sensitive applications, able to support the double of the input symbols of a standard DMT system [68].

7.1.1 Power efficient DHT-based optical OFDM scheme for IM/DD systems

DMT is a multi-carrier transmission technique where the OFDM signal is real-valued. No in phase and quadrature modulation onto an RF carrier is required and the complexity of the electronic design is reduced.

To generate real OFDM symbols, the input signal mapped into a complex constellation, generally *m*-QAM (quadrature amplitude modulation) is forced to have Hermitian symmetry.

We have demonstrated that when using the DHT, in place of the discrete Fourier transform (DFT), Hermitian symmetry constraint is not required, resulting in a simpler implementation. In fact, if the constellation used is real (such as BPSK or *M*-PAM), the transmitted signal, i.e. the inverse DHT of a sequence *x(n)*

$$h(k)=\frac{1}{\sqrt{N}}\sum_{n=0}^{N-1}x(n)\left[\cos(2\pi kn/N)+\sin(2\pi kn/N)\right] \qquad k=0,1,\cdots,N-1$$

is real and all the DHT points support independent information data, as shown in Figure 44.

Therefore, in order to transmit the same information bit sequence per parallel processing as a standard DMT system, with DHT modulation a lower real constellation size is required. Moreover, minimum arithmetic complexity algorithms can be applied and the computational time required in DMT systems for the complex conjugate vector calculation is saved. The same digital signal processing (DSP) can be used for modulation and demodulation, since DHT is self-inverse. As in standard DMT systems, only one single digital-to-analog converter (DAC) and a single analog-to-digital converter (ADC) are required.

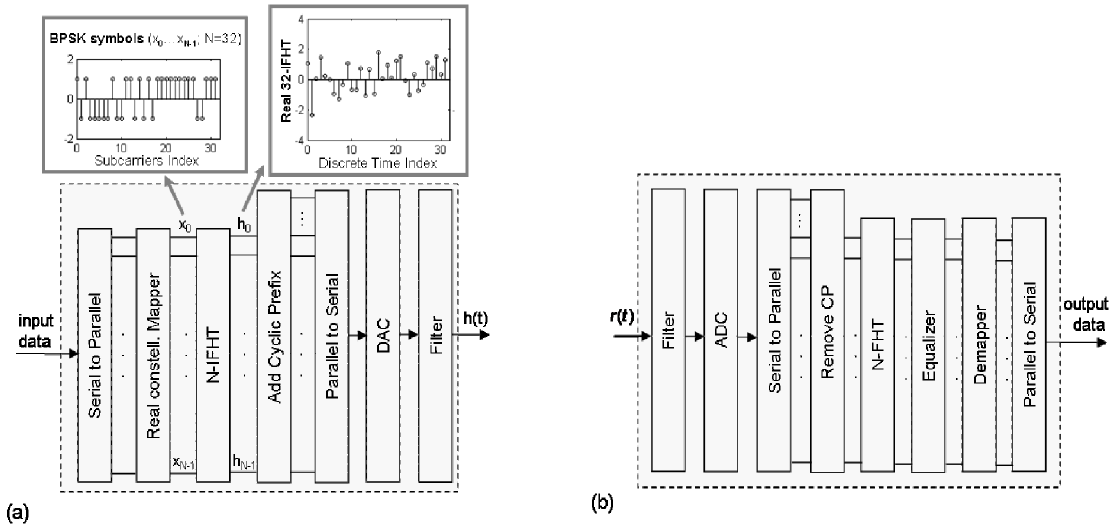

Figure 44. FHT-based OFDM (a) transmitter and (b) receiver. In the insets, 32 BPSK input symbols and corresponding real-valued IFHT.

A real OFDM signal to be transmitted on an intensity-modulated (IM) system must be converted into positive. This can be obtained by either adding a DC bias or asymmetrically clipping (AC) the OFDM signal. With a suitable choice of the subcarriers to be modulated, AC technique allows transmitting positive OFDM signals without clipping noise, resulting in a power efficient solution.

We have demonstrated that both DC-biased and AC techniques can be applied to OFDM signals generated by DHT, with the advantage of providing a simpler system with low computational complexity [68].

When AC is adopted, only the odd subcarriers are modulated and the OFDM signal can be clipped at zero level without losing information. All the clipping noise falls into the even subcarriers; the symbol sequence can be recovered from the odd subcarriers and the constellation points have the half of the original values, as indicated in Figure 45. The inset shows the received constellation in a back-to-back system using BPSK.

Clipping is also required when DC-biased solution is adopted. In fact, if the OFDM signal has high negative picks, although a bias is added, residual negative peaks can be present in the biased signal, that have to be clipped at zero level for IM. Therefore, an additional noise component affects the signal and, depending on the clipping level, it can severely degrade the transmission.

AC and DC-biased techniques trade power and bandwidth efficiency. Indeed, when AC is applied, the electrical signal (proportional to the optical power) results considerably reduced compared to the DC-biased case, even if a minimum bias value is considered, as shown in Figure 45. However, AC technique requires the double of carriers to transmit the same data per parallel processing of the DC-biased implementation.

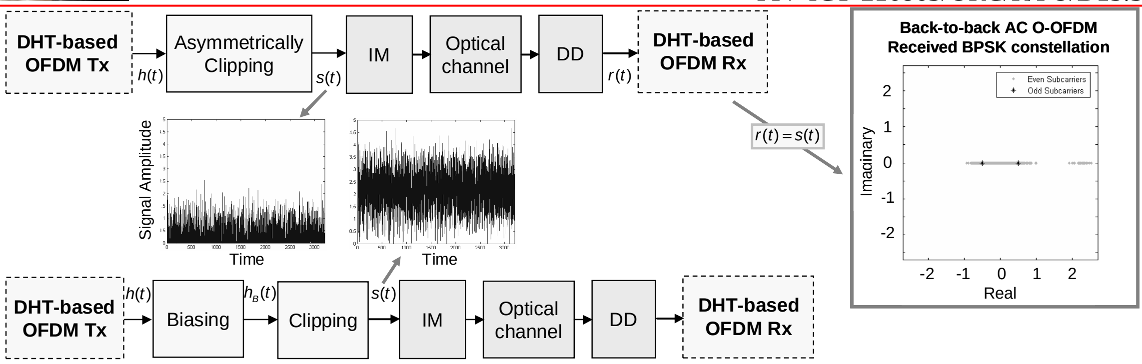

Figure 45. AC (top) and DC-biased (bottom) O-OFDM IM/DD systems. Asymmetrically clipped and biased signals of 50 OFDM symbols with BPSK and N=64-DHT.

7.1.2 Performance of DHT-based optical OFDM systems

We have evaluated the performance in additive white Gaussian noise (AWGN) channel to furnish an analysis of the DHT-based system in comparison with FFT-based system.

The BER curves of Figure 46 can be obtained with FFT-based O-OFDM using complex larger size constellations [69]: the same data rate transmitted with BPSK, 4-PAM and 8-PAM requires 4, 16 and 64-QAM, if FFT is used.

In AC technique, only *N/4* of the *N* FFT subcarriers support data symbols, while the available subcarriers of an N-order DHT are *N/2*. DC-biased solution uses the double of carriers (even and odd) to transmit data, but requires higher bit electrical energy normalized to the noise power spectral density ($E_{b(elec)}/N_0$), as shown in Figure 46. Similarly to FFT-based O-OFDM, the corresponding normalized bit optical power can be easily derived, evidencing the superior power efficiency of AC [68]. 7dB and 13dB bias are added to the OFDM signal; a larger bias ensures lower clipping noise, but requires higher electrical and optical power for transmitting the same constellation symbols. When 4-PAM format is supported by a system using 7dB bias value (corresponding to the double of the signal standard deviation), the system performance is affected by high clipping noise; the same can be observed in FFT-based system supporting 16-QAM and using the same bias value [69].

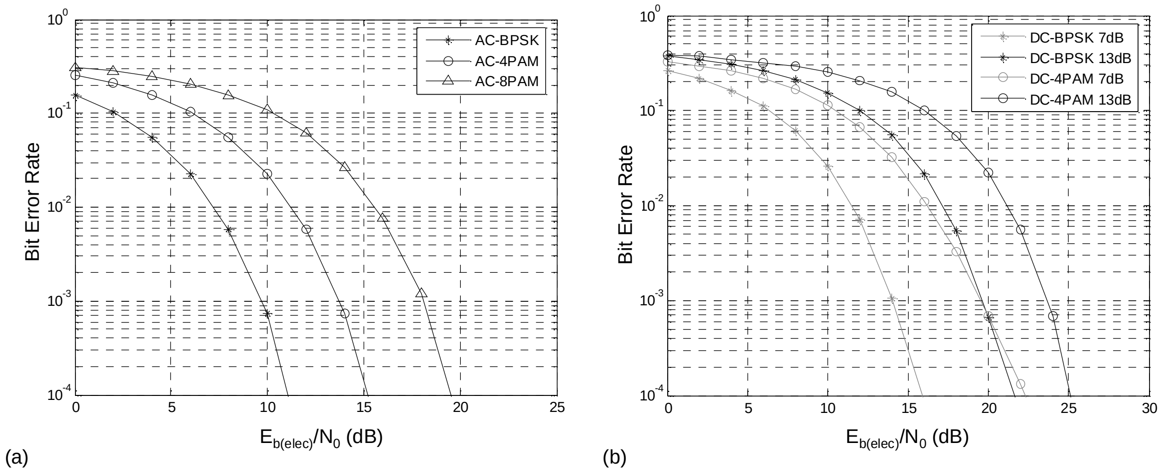

Figure 46. Performance of (a) AC and (b) DC-biased O-OFDM based on DHT in AWGN channel.

7.2 Polarisation-dependent properties of fibre Bragg gratings (UMons, UPVLC)

In the frame of the WP15, FPMs/UMons together with UPVLC have studied both theoretically and experimentally the effect of polarization dependent properties of fiber Bragg gratings (FBGs).

During the standard FBG fabrication process, only one side of the optical fiber is usually exposed to the UV laser. As a result, the refractive index change is not constant through the fiber cross-section since it is larger at the core side facing the UV light. This non-uniformity of the refractive index profile causes photo-induced birefringence that combines with the intrinsic fiber birefringence to give a global birefringence value Δn.

Birefringence is defined as the difference in refractive index between a particular pair of orthogonal polarization modes (called the eigenmodes or modes x and y). The effective refractive indices of the two eigenmodes are defined by:

$$\mathrm{n}_{\mathrm{eff},x} = \mathrm{n}_{\mathrm{eff}} + \frac{\Delta n}{2}; \quad \mathrm{n}_{\mathrm{eff},y} = \mathrm{n}_{\mathrm{eff}} - \frac{\Delta n}{2} \tag{1}$$

where n_{eff} is the mean effective refractive index of the fiber core and Δn is the global birefringence value reached at the end of the writing process. n_{eff} and Δn are wavelength dependent but, because the investigated wavelength range is practically limited to the grating bandwidth, their wavelength dependency can be neglected.

In the presence of birefringence, since the eigenmodes undergo different couplings through the FBG, the transmission coefficient of an FBG degenerates into two coefficients corresponding to the x and y modes, respectively. In a Cartesian coordinates system whose reference axes match the FBG eigenmodes, the Jones matrix associated to the grating is diagonal and the Jones vector of the transmitted signal is then:

$$\begin{pmatrix} E_{t,x} \\ E_{t,x} \end{pmatrix} = \begin{pmatrix} t_x & 0 \\ 0 & t_y \end{pmatrix} \begin{pmatrix} E_{i,x} \\ E_{i,y} \end{pmatrix} = \begin{pmatrix} t_x E_{i,x} \\ t_y E_{i,y} \end{pmatrix} \tag{2}$$

$t_{x(y)}$ denotes the transmission coefficient of the FBG corresponding to the $x(y)$ mode. $(E_{i,x}\ E_{i,y})^{T}$ is the Jones vector of the input signal:

$$\begin{pmatrix} E_{i,x} \\ E_{i,y} \end{pmatrix} = \begin{pmatrix} M_x e^{j\xi_x} \\ M_y e^{j\xi_y} \end{pmatrix} \tag{3}$$

In Eq. (6), $M_{x(y)}$ and $\xi_{x(y)}$ are the amplitude and phase angle of the $x(y)$ component of the input signal, respectively. $t_{x(y)}$ is derived from the coupled mode theory:

$$t_{x(y)} = \frac{j\alpha_{x(y)}}{\sigma_{x(y)} \sinh\left(\alpha_{x(y)} L\right) + j\alpha_{x(y)} \cosh\left(\alpha_{x(y)} L\right)} \tag{4}$$

$\alpha_{x(y)}$ and $\sigma_{x(y)}$ correspond to the parameters α and σ defined in [70] where n_{eff} has been replaced by $n_{\mathrm{eff},x(y)}$ so that:

$$\alpha_{x(y)} = \sqrt{\kappa^2 - \sigma_{x(y)}^2}\ ; \quad \kappa = \frac{\pi \delta n_{eff}}{\lambda}\ ; \quad \sigma_{x(y)} = \frac{2\pi (n_{eff,x(y)} + \delta n_{eff})}{\lambda} - \frac{\pi}{\Lambda} \tag{5}$$

where δn_{eff} is the core refractive index modulation, L is the grating length, Λ is the periodicity and λ is the wavelength.

In practice, the order of magnitude of photo-induced birefringence typically varies between 10^{-6} and 10^{-5}. The spectral shift between $t_x(\lambda)$ and $t_y(\lambda)$ is given by $2\Delta n\Lambda$ and is then only a few picometers. Hence, the effect of Δn cannot be directly perceived in the transmitted spectrum because of the limited resolution of measurement devices. Δn can be enhanced by transversal loads and can reach values of the order of 10^{-4}, as in the case of polarization maintaining fibers. The photo-induced birefringence has a strong impact on the polarization dependent loss (PDL) and differential group delay (DGD) evolutions with wavelength.

PDL is defined as the maximum change in the transmitted power when the input state of polarization is varied over all polarization states. PDL is given by Eq. (6):

$$\mathrm{PDL}(\lambda) = 10\log_{10}\left(\frac{T_{\max}(\lambda)}{T_{\min}(\lambda)}\right) \tag{6}$$

where $T_{\max}$ and $T_{\min}$ denote the maximum and minimum power transmitted through the optical component. In the case of FBGs, it is easy to show that Eq. (6) degenerates into Eq. (7) in which $T_{x(y)}(\lambda)$ is equal to $|t_{x(y)}(\lambda)|^2$ [71]:

$$\mathrm{PDL}(\lambda) = 10\log_{10}\left(\frac{T_x(\lambda)}{T_y(\lambda)}\right) \tag{7}$$

Figure 47 presents the typical PDL evolution for a 1 cm long uniform FBG computed using the previous equations.

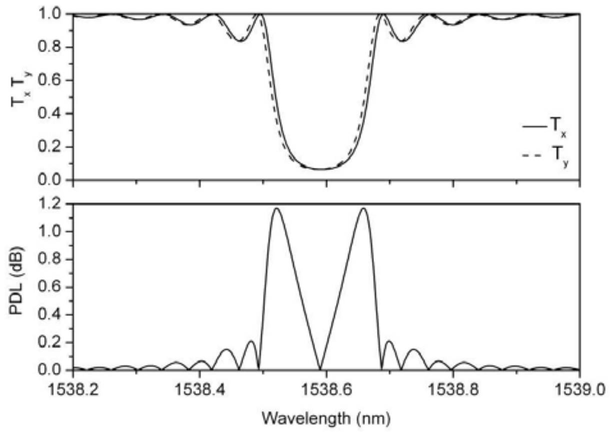

Figure 47: Transmitted spectrum and PDL curve for a 1 cm long uniform FBG (Parameters used for the simulation: L = 10 mm, Λ = 530 nm, δneff = 10-4 and Δn = 5 10-6).

The PDL evolution can be fully justified from the transmitted spectra corresponding to the x and y modes. Indeed, null PDL values are reached at wavelengths λ_i for which $T_x(\lambda_i)=T_y(\lambda_i)$. In

particular, it happens in the center of the rejection band. Between two consecutive minimum values, PDL evolutions exhibit local maximum values at wavelengths λ_j corresponding to the local maximum differences of amplitude between $T_x(\lambda_j)$ and $T_y(\lambda_j)$.
The greatest PDL values are obtained at the edges of the rejection band where the difference of amplitude between $T_x(\lambda)$ and $T_y(\lambda)$ is also the largest. In the remaining of the text, these values are called maximum PDL values. DGD is defined as the difference in group delay between the two eigenmodes:

$$\mathrm{DGD}(\lambda) = |\tau_x(\lambda) - \tau_y(\lambda)| \tag{8}$$

where $\tau_{x(y)}$ is the derivative of the $t_{x(y)}$ phase:

$$\tau_{x(y)}(\lambda) = \frac{-\lambda^2}{2\pi c}\frac{d}{d\lambda} arg\left(t_{x(y)}(\lambda)\right) \tag{9}$$

A typical DGD evolution is presented in Figure 48. It was obtained by implementing Eq. (8) and (9). Null DGD values are obtained at wavelengths λ_i for which $\tau_x(\lambda_i)=\tau_y(\lambda_i)$ whereas DGD maxima correspond to wavelengths λ_j for which the difference of amplitude between $\tau_x(\lambda_j)$ and $\tau_y(\lambda_j)$ is the greatest. These values are called maximum DGD values in the remaining.

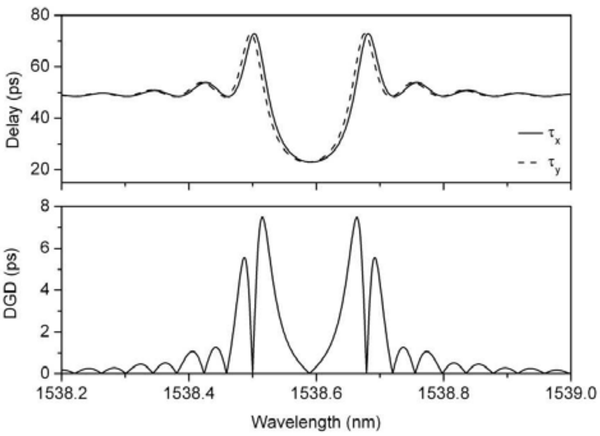

Figure 48: DGD curve for a 1 cm long uniform FBG (Parameters used for the simulation: L = 10 mm, Λ = 530 nm, δneff = 10-4 and Δn = 5 10-6).

Using the above mentioned equations, the impact of some FBG parameters (physical length and refractive index modulation profile) and the birefringence value on the wavelength evolutions of PDL and DGD have been analyzed and confirmed by experimental results obtained on FBGs written in photosensitive singlemode fiber [72, 73, 74]. Different techniques have also been reported to decrease the effect of the birefringence [75, 76].

8. Conclusions

This document has reported the progress that has been achieved during the third and final year of VCE-T. The main joint effort in the VCE is the compilation of a book; this effort is in its closing stages and will be completed with the publication of the book shortly after the end of the project. At the same time, a significant number of joint activities have been initiated, continued and carried out within the third year of the project. The main outcomes of these activities have been outlined in this report.

9. References

[1] M. Cavallari, C.R.S. Fludger, P.J. Anslow, "Electronic Signal Processing for Differential Phase Modulation Formats," in Proc. of OFC 2004, Los Angeles (CA), Feb. 2004, paper TuG2.

[2] M.S. Alfiad, et al., "Dispersion tolerant 21.4-Gb/s DQPSK using simplified Gaussian Joint-SymbolMLSE," in Proc. of OFC 2008, San Diego (CA), Feb. 2008, paper OThO3.

[3] T. Kupfer, C. Dorschky, M. Ene, S. Langenbach, "Measurement of the Performance of 16-States MLSE Digital Equalizer with Different Optical Modulation Formats," Proc. of OFC 2008, paper PDP13, San Diego, CA, USA, Mar. 2008.

[4] R.A. Griffin, A.C. Carter, "Optical differential quadrature phase-shift key (oDQPSK) for high capacity optical transmission," Proc. of OFC 2002, Anaheim (CA), 17-22 Mar 2002, pp. 367-368.

[5] D. van den Borne, E. Gottwald, G.D. Khoe, H. de Waardt, "Pseudo-Random Sequences for Modeling of Quaternary Modulation Formats," Proc. of OECC/IOOC2007, Pacifico Yokohama, July 2007, paper 13P-10.

[6] J. G. Proakis, "Digital Communication," Mc.Graw-Hill, New York, (1989).

[7] P. Poggiolini, G. Bosco, "Long-Haul Multi-Channel IMDD Transmission at 10.7 Gbit/s in a Dispersion-Managed Multispan System Using aMLSE Receiver," IEEE J. Lightw. Technol. , vol. 26, no. 17, pp. 3041-3047, Sep. 2008.

[8] A.V.T. Cartaxo, "Cross-phase modulation in intensity modulation-direct detection WDM systems with multiple optical amplifiers and dispersion compensators", J. Lightw. Technol., vol. 17, no. 2, Feb 1999, pp. 178-190.

[9] Y. Ma, Q. Yang, Y. Tang, S. Chen and W. Shieh, "1-Tb/s per Channel Coherent Optical OFDM Transmission with Subwavelength Bandwidth Access", in Proc. OFC 2009, post-deadline paper PDPC1, San Diego (USA), March 22-26 2009.

[10] S. Chandrasekhar, X. Liu, B. Zhu and D. W. Peckham, "Transmission of a 1.2 Tb/s 24-carrier No-Guad-Interval Coherent OFDM Superchannel over 7200-km of Ultra-Large-Area Fiber", in Proc. ECOC 2009, post-deadline paper PD2.6, Vienna (Austria), Sept. 20-24 2009.

[11] G. Gavioli et al., “Investigation of the Impact of Ultra-Narrow Carrier Spacing on the Transmission of a 10-Carrier 1 Tb/s Superchannel”, in Proc. OFC 2010, paper OThD3, San Diego (USA), March 21-25 2010.
[12] A. Carena, V. Curri, P. Poggiolini, F. Forghieri, “Dispersion Compensation and Mitigation of Non-Linear Effects in 111 Gb/s WDM Coherent PM-QPSK Systems,” IEEE Photonics Technology Letters, vol. 20, no. 17, pp. 1473-1475, Sept. 1st 2008.
[13] C. Behrens, R.I. Killey, S.J. Savory, M. Chen and P. Bayvel, “Fibre Nonlinearities in WDM-Systems with Reduced Channel-Spacing and Symbol-Rate”, in Proc. 36th European Conference on Optical Communication ECOC 2010, poster 4.20, Torino, Italy, September 2010.
[14] G. Golfarb and G. Li, “Efficient backward-propagation using wavelet-based filtering for fiber backward-propagation”, Optics Express, vol. 17, pp 8815-8821, 2009.
[15] I. Fatadin, D. Ives and S. J. Savory, “Blind equalization and carrier phase recovery in a 16-QAM Optical Coherent System”, IEEE Journal of Lightwave Technology, vol. 27, pp 3042-3049, 2009.
[16] A. Viterbi and A. Viterbi, “Nonlinear estimation of PSK-modulated carrier phase with application to burst digital transmission”, Transactions on Information Theory, vol. 29, pp 543-551, 1983.
[17] D.S. Millar et al., “Mitigation of Fiber Nonlinearity using a Digital Coherent Receiver”, IEEE Journal of Selected Topics in Quantum Electronics, vol. 16, pp 1217-1226, May 2010.
[18] M.Zitelli, F.Matera, M.Settembre, Journal of Lightwave Technology 17, (1999) 2498.
[19] P. J. Winzer, R. J. Essiambre, Proc. of IEEE vol. 94, n. 5, (2006) 952.
[20] A. Mecozzi, C. B. Clausen, and M. Shtaif, “Analysis of intra–channel nonlinear effects in highly dispersed pulse transmission in optical fibers,” IEEE Photonics Technology Letters, Vol. 12, No. 4, pp. 392–394, April 1, 2000.
[21] A. Mecozzi, C. B. Clausen, M. Shtaif, Sang–Gyu Park, and A. H. Gnauck, “Cancellation of timing and amplitude jitter in symmetric links using highly dispersed pulses,” IEEE Photon. Technol. Lett., vol. 13, No. 5, pp. 445–447, May 1, 2001.
[22] A. Mecozzi, C. Balslev Clausen, M. Sharif, IEEE Photonics Technology Letters vol. 12, no. 12, 2000, p. 1633.
[23] J. C. Geyer, et al., ”Channel Parameter Estimation for Polarization”, IEEE Photon. Technol. Lett., vol. 20, no. 18, pp. 776-778, May. 2008.
[24] F.Parmigiani, et al., “All-Optical Phase Regeneration of 40 Gbit/s DPSK Signals in a BlackBox Phase Sensitive Amplifier”, in Proc Optical Fiber Communication Conference (OFC/NFOEC 2010), San Diego (USA) Paper PDPC3, (2010).
[25] R. Phelan, B. Kelly, J. O’Carroll, C. Herbert, A. Duke and J. O’Gorman. “Room-Temperature Operation of Discrete-Mode InGaAs–AlAsSb Quantum-Cascade Laser With Emission at λ=3.3nm,” IEEE Electronics Letters, 45, 43-45, (2009)
[26] M.N. Petersen, “Performance Monitoring in the Next Generation of Optical Networks”, Proc. of . International Conference on Photonics in Switching 2006, Herakleion, Crete, Greece, 16-1

8 Oct. 2006.

[27] F.N. Hauske, M. Kuschnerov, B. Spinnler, B. Lankl, “Optical Performance Monitoring in Digital Coherent Receivers”, J. Lightwave Technol., vol. 27, no. 16, pp. 3623-3631, Aug. 2009.

[28] J. P. Gordon, and L. F. Mollenauer, “Phase noise in photonic communications systems using linear amplifiers,” Opt. Lett. 15(23), 1351–1353 (1990).

[29] A. Demir, “Nonlinear phase noise in optical-fiber-communication systems,” J. Lightwave Technol. 25 (8), 2002-2031 (2007).

[30]K. Cvecek, K. Sponsel, C. Stephan, G. Onishchukov, R. Ludwig, C. Schubert, B. Schmauss, and G. Leuchs, “Phase-preserving amplitude regeneration for a WDM RZ-DPSK signal using a nonlinear amplifying loop mirror,” Opt. Express 16, 1923-1928 (2008).

[31] K. Croussore, et al., Electron. Lett., 43 (3), 177 – 178, (2007).

[32]Masayuki Matsumoto and Kenichi Sanuki, “Performance improvement of DPSK signal transmission by a phase-preserving amplitude limiter,” Opt. Express 15, 8094-8103 (2007).

[33] M. Matsumoto et al., Opt. Express 16, 11169-11175 (2008).

[34] K. Croussore, et al., Opt. Express, 14, 2085-2094 (2006).

[35] K. Croussore et al., IEEE/LEOS Winter Topical Meeting Series, MB1.3, (2008).

[36] K. Croussore et al., IEEE Phot. Technol. Lett., 19 (11), 864-866, (2007).

[37] F.Parmigiani, R.Slavik, J.Kakande, L.Gruner-Mielsen, D.Jakobsen, S.Herstrom, S.Weerasuriya, S.Sygletos, A.D.Ellis, P.Petropoulos, D.J.Richardson, “All-optical phase and amplitude regeneration properties of a 40 Gbit/s DPSK black-box phase sensitive amplifier, “ ECOC 2010 Turin 9-23 Sep 2010.

[38] R. Weerasuriya, et al., Proc. OFC’10, OWT6 (2010).

[39] M. Sjödin, et al., “Cancellation of SPM in Self-Homodyne Coherent Systems,” ECOC 2009, paper We8.4.5.

[40] Sköld, et. al., “Constellation diagram analysis of DPSK signal regeneration in a saturated parametric amplifier”, Opt. Express 16, 5974-5982 (2008).

[41] E. Ip et. al., Opt. Express 16, 753-791 (2008).

[42] K. Roberts et. al., J. Lightwave Technol. 27, 3546-3559 (2009).

[43] M. Vasilyev, Opt. Exp., 13, 7563 (2005).

[44] M. Matsumoto, Opt. Express 18, 10-24 (2010).

[45] Z. Zheng et. al., Optics Communications 281, 2755-2759 (2008).

[46] K. Croussore, I. Kim, Y. Han, C. Kim, G. Li, and S. Radic, “Demonstration of phase-regeneration of DPSK signals based on phase-sensitive amplification,” Opt. Express, 13, 3945-3950 (2005).

[47] R. Slavik, et. al., "All-optical phase and amplitude regenerator for next-generation telecommunications systems," Nat Photon 4, 690-695 (2010).

[48] Z. Zheng, L. An, Z. Li, X. Zhao, and X. Liu, "All-optical regeneration of DQPSK/QPSK signals based on phase-sensitive amplification," Optics Communications 281, 2755-2759 (2008).

[49] M. Vasilyev, "Distributed phase-sensitive amplification," Opt. Express 13, 7563-7571 (2005).

[50] J.Kakande, A.Bogris, R.Slavik, F.Pamigiani, D.Syvridis, P.Petropoulos, and D.J.Richardson, “First demonstration of all-optical QPSK signal regeneration in a novel multi-format phase sensitive amplifier”, in Proc. of ECOC 2010, Turin (Italy), Sept. 2010, post deadline PD 3.3

[51] C. Yu, S. Zhang, P. Kam, and J. Chen, "Bit-Error Rate Performance of Coherent Optical M-ary PSK/QAM using Decision-Aided Maximum Likelihood Phase Estimation," Opt. Express 18, 12088-12103 (2010).

[52] J. Hult: A fourth-order Runge-Kutta in the interaction picture method for simulation supercontinuum generation in optical fibers, J. Lightwave Technol., vol. 25, pp. 3770-3775, 2007.

[53] P.V. Mamyshev: All-optical data regeneration based on self-phase modulation effect, in Proc. ECOC, 475-476, 1998.

[54] D. Bolt and K. Ennser, “Investigation of multiple passes through a double-cell self-phase modulation based regenerator”, in Proc. International Conference on Transparent Optical Networks – ICTON’10, Munich, Germany, 2010, paper We.P.10.

[55] S. Taccheo and K. Ennser, “Investigation of Amplitude Noise and Timing Jitter of Supercontinuum Spectrum Sliced Pulses,” IEEE Photon. Technol. Lett., vol. 10, no. 8, pp. 1100-1102, 2002.

[56] L. Provost, C. Finot, K. Mukasa, P. Petropoulos, and D.J. Richardson: Design scaling rules for 2R-optical self-phase modulation-based regenerators, Optics Express, vol. 15, pp. 5100-5112, 2007.

[57] L. Provost, C. Finot, K. Mukasa, P. Petropoulos and D.J. Richardson: Generalisation and experimental validation of design rules for self-phase modulation-based 2R-regenerators, in Proc. OFC/NFOEC, 2007.

[58] A.G. Striegler and B. Schmauss: Analysis and optimisation of SPM-Based 2R signal regeneration at 40Gb/s, J. Lightwave Technol., vol. 24, pp. 2835-2842, 2006.

[59] C. Floridia, M. Rocha, J. de Moraes, and E. Bezerra, “High accuracy and fast acquisition time of a polarisation nulling-based OSNR monitor,” Electronics Letters, vol. 46, no. 2, p. 152, 2010.

[60] J. Montalvo, D. S. Montero, C. Vázquez, J. M. Baptista, J. L. Santos“Radio-Frequency Self-Referencing System for Monitoring Drop Fibres in WDM Passive Optical Networks” IET Optoelectronics, vol. 4, no. 6, Special issue in Next Generation Optical Access, 2010.

[61] M.N. Petersen, “Performance Monitoring in the Next Generation of Optical Networks”, Proc. of . International Conference on Photonics in Switching 2006, Herakleion, Crete, Greece, 16-18 Oct. 2006.

[62] F.N. Hauske, M. Kuschnerov, B. Spinnler, B. Lankl, “Optical Performance Monitoring in Digital Coherent Receivers”, J. Lightwave Technol., vol. 27, no. 16, pp. 3623-3631, Aug. 2009.

[63 J. Montalvo, Kivilcim Yüksel, D.S. Montero, Marc Wuilpart, Patrice Mégret, C. Vazquez “New Radio-Frequency Techniques for Individual Drop Fibre Monitoring and Temperature Sensing in PONs” ONDM 2011 Bolonia (Italy) February 2011.

[64] W. Shieh, I. Djordjevic, OFDM for Optical Communications, Elsevier, USA, 2010.

[65] S. C. J. Lee, F. Breyer, S. Randel, H. P. A. van den Boom, and A. M. J. Koonen, “High-speed transmission over multimode fiber using discrete multitone modulation,” J. Opt. Networking, vol. 7, pp. 183-196, 2008.

[66] J. M. Tang, and K. L. Shore, “Maximizing the transmission performance of adaptively modulated optical OFDM signals in multimode-fiber links by optimizing analog-to-digital converters”, J. Lightwave Technol., vol. 25, pp. 787-798, 2007.

[67] Y. Benlachtar, R. Bouziane, R.I. Killey, C.R. Berger, P. Midler, R. Koutsoyannis, J.C. Hoe, M. Puschel, and M. Glick, “Optical OFDM for the data center,” in Proc. Int. Conf. Transparent Optical Networks 2010 (ICTON 2010), Paper We.A4.3.

[68] M. Svaluto Moreolo, R. Muñoz, G. Junyent, “Novel power efficient optical OFDM based on Hartley transform for intensity modulated direct detection systems”, IEEE/OSA Journal of Lightwave Technology, Vol. 28, No. 5, pp. 798-805, March 2010.

[69] J. Armstrong, B. J. C. Schmidt, “Comparison of asymmetrically clipped optical OFDM and DC-biased optical OFDM in AWGN,” IEEE Commun. Lett., vol. 12, pp. 343–345, May 2008.

[70] T. Erdogan, ‘Fiber grating spectra’, Journal of Ligthwave Technology, vol. 15, n. 8, pp. 1277-1294, 1997.

[71] S. Bette, C. Caucheteur, M. Wuilpart, P. Mégret, “Theoretical and experimental study of differential group delay and polarization dependent loss of Bragg gratings written in birefringent fiber”, Optics Communications, vol. 269, pp. 331-337, 2007.

[72] S. Bette, C. Caucheteur, M. Wuilpart, P. Mégret, R. Garcia Olcina, S. Sales, J. Capmany, “Spectral characterization of differential group delay in uniform fiber Bragg gratings”, Optics Express, vol. 13, n. 25, pp. 9954-9960, 2005.

[73] C. Caucheteur, S. Bette, R. Garcia Olcina, M. Wuilpart, S. Sales, J. Capmany, P. Mégret, “Influence of the Grating Parameters on the Polarization Properties of Fiber Bragg Gratings”, IEEE Journal of Lightwave Technology, vol. 48, n. 9, pp. 1635-1641, 2009.

[74] S. Bette, C. Caucheteur, R. Garcia-Olcina, M. Wuilpart, S. Sales, J. Capmany, “Relationship between chromatic dispersion and differential group delay in weakly birefringent fiber gratings”, IEEE Photonics Technology Letters, vol. 20, n.5, pp. 437-439, 2008.

[75] V. García-Muñoz, C. Caucheteur, S. Bette, M. Wuilpart, M. Muriel, P. Mégret, “Reduction of polarization related effects in superimposed fiber Bragg gratings”, Applied Optics, vol. 48, n. 9, pp. 1635-1641, 2009.

[76] S. Bette, C. Caucheteur, V. Garcia-Munoz, R. Garcia-Olcina, M. Wuilpart, S. Sales, J. Capmany, P. Mégret, “PDL and DGD reduction in Bragg gratings using twisted fibers for the inscription”, IEEE Photonics Technology Letters, vol. 21, n. 22, pp. 1689-1691, 2009.

Table of Figures